Increasing Antarctic snowfall mitigates sea level rise less than projected due to meltwater influence on sea surface temperatures

David P Schneider[1,2], Ziqi Yin[3], Gemma K. O'Connor[3], Edward Blanchard-Wrigglesworth[3], Zaria I Cast[4], Rajashree Datta[3], and Zachary Espinosa[3]

[1]Cooperative Institute for Research in Environmental Sciences, University of Colorado -Boulder
[2]Climate and Global Dynamics Laboratory, National Center for Atmospheric Research
[3]Affiliation not available
[4]Department of Geography, University of Colorado -Boulder

August 24, 2024

Abstract

Ice-core-based reconstructions show that increased snow accumulation on the Antarctic Ice Sheet mitigated global sea level rise by ~ 10 mm during 1901-2000 (*Medley and Thomas*, 2019). Here, we attribute this trend by evaluating a suite of single-forcing, all-forcing and nudged ensembles from a climate model, along with dynamically consistent reconstructions of sea level pressure, temperature and wind from paleoclimate data assimilation (PDA). The single-forcing ensembles reveal that rising concentrations of greenhouse gasses (GHGs) have been the dominant driver of the historical snow accumulation increase, but acting alone, GHGs would have caused twice the observed increase. We investigate possible explanations for this over-prediction: a) The uncertain cooling effects of anthropogenic aerosols; b) Extreme internal variability; c) Atmospheric circulation trends; and d) Sea surface temperature (SST) trends evident in the PDA reconstructions (and observed SSTs) but not simulated by the model. The latter best explains the spatial and temporal evolution of snow accumulation, including the lack of an Antarctic-wide accumulation increase since 1980. This SST trend pattern resembles the previously modeled response to Antarctic meltwater, and its emergence coincides with the mid-Twentieth-Century onset of ice shelf thinning and retreat of Thwaites and Pine Island glaciers. Aerosols have also damped the accumulation increase and contributed to the global-scale SST pattern, which includes long-term cooling in the central tropical Pacific that cannot be explained by internal variability. Our results imply that including Antarctic meltwater in models would substantially improve projections of Antarctic snowfall, global sea level, and SSTs in the Southern Ocean and tropical Pacific.

Abstract content goes here

Increasing Antarctic snowfall mitigates sea level rise less than projected due to meltwater influence on sea surface temperatures

David P. Schneider*[a,b]; Ziqi Yin[c]; Gemma K O'Connor[d] ; Edward Blanchard-Wrigglesworth[e]; Zaria I. Cast[f]; Rajashree Tri Datta[c]; Zachary I. Espinosa[e]

a. Cooperative Institute for Research in Environmental Sciences, University of Colorado – Boulder, Boulder, CO 80309 USA

b. Climate and Global Dynamics Laboratory, National Center for Atmospheric Research, Boulder, Colorado, 80305 USA

c. Department of Atmospheric and Oceanic Sciences, University of Colorado – Boulder, CO 80309 USA

d. School of Oceanography, University of Washington, Seattle, WA 98195 USA

e. Department of Atmospheric Sciences, University of Washington, Seattle, WA 98195 USA

f. Department of Geography, University of Colorado – Boulder, Boulder, CO 80309 USA

*Corresponding Author: David P. Schneider
email: David.Schneider-1@colorado.edu

ABSTRACT

Ice-core-based reconstructions show that increased snow accumulation on the Antarctic Ice Sheet mitigated global sea level rise by ~ 10 mm during 1901-2000 (*Medley and Thomas*, 2019). Here, we attribute this trend by evaluating a suite of single-forcing, all-forcing and nudged ensembles from a climate model, along with dynamically consistent reconstructions of sea level pressure, temperature and wind from paleoclimate data assimilation (PDA). The single-forcing ensembles reveal that rising concentrations of greenhouse gasses (GHGs) have been the dominant driver of the historical snow accumulation increase, but acting alone, GHGs would have caused twice the observed increase. We investigate possible explanations for this over-prediction: a) The uncertain cooling effects of anthropogenic aerosols; b) Extreme internal variability; c) Atmospheric circulation trends; and d) Sea surface temperature (SST) trends evident in the PDA reconstructions (and observed SSTs) but not simulated by the model. The latter best explains the spatial and temporal evolution of snow accumulation, including the lack of an Antarctic-wide accumulation increase since 1980. This SST trend pattern resembles the previously modeled response to Antarctic meltwater, and its emergence coincides with the mid-Twentieth-Century onset of ice shelf thinning and retreat of Thwaites and Pine Island glaciers. Aerosols have also damped the accumulation increase and contributed to the global-scale SST pattern, which includes long-term cooling in the central tropical Pacific that cannot be explained by internal variability. Our results imply that including Antarctic meltwater in models would substantially improve projections of Antarctic snowfall, global sea level, and SSTs in the Southern Ocean and tropical Pacific.

SINGIFICANCE

The Antarctic Ice Sheet (AIS) is losing ice at its margins, raising global sea level. Physical theory predicts that some of this sea level impact would be mitigated if there is more snow accumulation on the AIS from increased snowfall with warmer temperatures. However, evidence from historical data and model experiments has been inconclusive. Using a novel combination of model experiments and reconstructions, we demonstrate that greenhouse gasses have been the dominant cause of increased AIS snow accumulation, yet the measured increase in accumulation is less than the model predicts. Our results indicate that this discrepancy can be explained by the cooling influence of meltwater from ice loss on sea surface temperatures, an effect not included in most model experiments.

Keywords/phrases: Antarctic surface mass balance | Precipitation response to climate change | Global sea level rise | Global teleconnections | Climate change attribution | Antarctic meltwater | SST pattern effect

[MAIN TEXT]

The Antarctic Ice Sheet (AIS) is losing mass, primarily via enhanced ice discharge induced by ice-shelf basal melting, contributing to global sea level rise (1 - 5). The rate of mass loss has generally been accelerating since the 1980s (3, 5), but gravity anomalies from satellite data suggest that changes in snow accumulation have modulated this rate, even slowing it down during 2016-2019 (4). Snow accumulation is the only mass input to the AIS; its time-averaged value is ~ 2000 Gt/y over the grounded AIS (6), or ~ 6 mm of sea level equivalence (SLE). As such, modest changes to the snow accumulation rate, especially when sustained over multiple years, affect the overall mass balance of the AIS and its contribution to sea level. In the short term, an increase in snow accumulation represents an increase in mass storage on the AIS, thereby removing this mass from the ocean and causing a relative lowering of sea level.

Climate model projections suggest that annual Antarctic snowfall (the dominant term in snow accumulation) could increase by up to 43% during the 21st Century (7) highlighting a potentially significant, but highly uncertain role for changes in Antarctic snow accumulation to affect sea level rise. Given that AIS mass balance is the largest source of uncertainty in global sea level projections for the 21st Century (5), better constraining the mass input from snow accumulation is scientifically and societally important. Although here we focus on the immediate potential sea level mitigation from increased Antarctic snow accumulation, over multiple decades to centuries, increased mass input may enhance the driving stress of outlet glaciers, accelerating their discharge of ice into the ocean (8). Current-generation climate models represent snow accumulation on the AIS, but do not represent the dynamic coupling of the AIS to the ocean. They omit the freshwater fluxes from ice discharge and basal melting, which we will argue play a crucial role in shaping the sea surface temperature (SST) trend patterns that in turn affect snow accumulation.

The thermodynamics encoded in climate models dictates that the moisture holding capacity of the atmosphere increases with warming, leading to the expectation that snowfall also increases (5). From the past ~ 60 years of station-based observations, the Antarctic surface and troposphere have significantly warmed (9, 10), while temperatures have remained below freezing most of the time, suggesting that snow accumulation may also have increased. However, measuring precipitation and snow accumulation in Antarctica is notoriously difficult, and few, reliable, long-term *in situ* observational records exist. To estimate surface mass input for mass balance studies, a common approach is to force a polar regional climate model at its lateral boundaries with data from global atmospheric reanalysis, while lower boundary conditions, SSTs and sea ice concentrations, are prescribed (11, 12). These reanalysis and regional model studies have found no significant change in Antarctic snow accumulation since 1979 (11, 12, 13). Although precipitation trends in reanalysis can be unreliable (14), real climatic factors could explain the lack of an upward snow accumulation trend. These include the observed surface cooling of the Southern Ocean (15, 16), increased Antarctic sea ice extent during 1979-2014 (17), and strengthening of the circumpolar westerly winds (1, 18). Other studies argue that the interannual- to decadal- scale variability of precipitation is large enough to mask a warming-driven precipitation increase in the short historical record (19).

Despite the challenges in measuring snow accumulation and detecting significant change, nature may be providing dramatic clues as to the future of snow accumulation on the AIS. 2022 was a record-setting year for Antarctic precipitation (as estimated by reanalysis since 1979), associated with an exceptionally large atmospheric river event and heat wave (13, 20). Ice-core based studies have found increases in the annual accumulation rate on century timescales, especially in the Antarctic Peninsula and Queen Maud Land (QML) regions (21, 22). However, the spatial sampling of ice cores is too limited to directly infer changes in AIS-wide snow accumulation. To obtain a more complete spatial-temporal dataset that represents the entire AIS, statistical approaches have combined temporal information from ice cores with spatial relationships from models or reanalysis (1, 2, 23). The earliest of these studies found no significant increase in AIS snowfall over the 1957-2000 period (23). The more recent studies, using additional ice core networks and newer reanalyses, have reported significant increases, ranging from ~ 10 mm (1) to ~ 14 mm (2) SLE over the 20th Century. While the 20th Century accumulation trend is robust, the relative sea level mitigation has some dependence on the exact methodology used (2) and the estimate of the baseline accumulation rate (24).

Importantly, the two newer statistical reconstructions (1, 2) bring observations more in line with expectations from thermodynamics and climate models. To date, there has been little attention given to evaluating the quantitative agreement between these reconstructions and climate models, nor to attributing the changes to specific climate forcings, such as changes in greenhouse gasses, aerosols, and stratospheric ozone. Such evaluations and attributions are critical for understanding the climatic factors that affect the AIS and for gaining confidence in model-based projections of AIS snow accumulation and sea level. We are therefore motivated to evaluate the agreement between reconstructed snow accumulation and a current-generation climate model over the 20th Century, and to use the same model to assess the main drivers of historical change and constrain future projections.

We compare snow accumulation in a suite of CESM2 (25) experiments with the reconstruction of Medley and Thomas (1) (hereafter, 'MT19' or 'reconstruction'), as described in *Materials and Methods*, favoring this reconstruction because it is accessible, well verified and has been used in previous work with CESM2 (6). An advantage of CESM2 over other climate models is its good representation of the surface climate of Antarctica, including the processes that affect snow accumulation (6). Accumulation is estimated as the sum of the precipitation terms (snowfall and rain) minus the ablation terms of sublimation, evaporation, and surface meltwater runoff. We use the term "snow accumulation" for consistency with ref. (1) and to emphasize that snowfall is the only mass input to the AIS. "Surface mass balance (SMB)" has the same meaning, and our methods to obtain snow accumulation from CESM2 output are the same as ref (6). Our primary metric of snow accumulation is the timeseries of cumulative mass over the grounded AIS. This metric de-emphasizes the large temporal variability of precipitation (19), making for a less noisy data-model comparison, and permitting the time-integrated signals of climate forcings (26) to be more easily detected. The spatial pattern of snow accumulation trends is also a key indicator of the responsible climate drivers; this is adopted as a secondary metric for interpreting the Antarctic snow accumulation history.

A previous evaluation reported that CESM2 simulates an unrealistically large, upward trend in snow accumulation for the 1979-2015 period (6). This trend contributes to a positive bias in modern-day snow accumulation compared with estimates from regional models (12). The trend is in the forced response in an 11-member historical ensemble (25). As such, it does not reflect the many factors that can influence snow accumulation, especially the so-called SST "pattern effect", which arises from incorrectly simulated SST trend patterns, especially in the Southern Ocean and eastern Pacific, major moisture source regions for Antarctic snow (15, 16, 27, 28). Here, we leverage a much larger suite of CESM2 experiments, listed in Table 1, to explore a wider range of plausible histories and drivers of snow accumulation. As these ensembles all use the same physical climate model, they can be systematically compared to tease apart signals from the different influences on snow accumulation. The first four ensembles in Table 1 comprise the single-forcing large ensemble (29), which, added together, have the same external forcings as the half of the 100-member CESM2 Large Ensemble (CESM2-LE) that has smoothed biomass burning (30). The other half of the CESM2-LE uses the standard CMIP6 forcing, as do the rest of the CESM2 ensembles in Table 1.

Stratospheric ozone depletion is represented in the CESM2-LE, TPACE and EE ensembles, but its role cannot be specifically isolated in this framework, as was done in studies with CESM1 (31, 32). AIS meltwater effects (33, 34) are not explicitly included, as there are no relevant observations or experiments available covering the full 20th Century. However, an Antarctic meltwater "hosing" ensemble was conducted with CESM1 for 1980-2013 (34); we leverage these data as they provide insight into the possible influence of meltwater on SSTs and snow accumulation over the 20th Century.

A prominent criticism of CESM2 is its equilibrium climate sensitivity (ECS) of ~ 5 K, which is higher than most observationally constrained estimates (15), and may lead to more warming and Antarctic snow accumulation than observed (6). However, results from several recent experiments demonstrate that ECS is not of leading-order relevance in simulating the historical and near-future periods investigated here. Under GHG forcing only, CESM2 and CESM1 (ECS of ~ 4 K) simulate the same global-mean warming over 1920-2050 (29). Under the same suite of all CMIP5 forcings, they also simulate very similar global-mean warming (35, 36). Forcing scenario uncertainty between CMIP5 and CMIP6, particularly regarding aerosols, has a much greater impact on simulated warming than ECS (16, 25, 29, 35, 36). Moreover, the SST pattern effect makes high-ECS models appear to be wrong, even when they may not be, as the observed SST trends are compatible with a wide range of ECS values (15).

The MT19 dataset ends in 2000 due to its reliance on ice core records. To bring our evaluation closer to the present day, we utilize the ERA5 atmospheric reanalysis (37) as well as a CESM2 experiment in which the model's winds are nudged to winds from ERA5 across the middle and high southern latitudes, following a protocol developed with CESM1 (20, 38). To help visualize and quantify the role of atmospheric circulation over the entire 20th Century, we employ reconstructions of zonal winds, sea level pressure (SLP), and surface air temperature (SAT) generated by paleoclimate data assimilation (PDA). In addition to utilizing two of the previously published, CESM1-based reconstructions (18), we present a new reconstruction using data from the CESM2-LE as the prior to ensure consistency with the CESM2 and with CMIP6 forcing.

abbreviation	model	radiative forcing	SSTs, sea ice	major purposes	ensemble members
GHG	CESM2	anthropogenic greenhouse gasses	coupled	evaluate forced response to greenhouse gasses	15
AAER	CESM2	anthropogenic industrial aerosols (CMIP6)	coupled	evaluate forced response to CMIP6 anthropogenic aerosols	20 (15 for GHG + AAER)
BMB	CESM2	biomass burning aerosols (smoothed)	coupled	evaluate forced response to biomass burning	15
EE	CESM2	stratospheric & tropospheric ozone; solar variability; volcanic aerosols; EE = 'Everything Else'	coupled	evaluate forced response to forcings not included in above single-forcing ensembles	15
CESM2-LE	CESM2	Large Ensemble; all major radiative forcings from CMIP6, with smoothed biomass burning	coupled	evaluate response to combined forcings; separate forced response from internal variability	50
CESM2-LEcmip6	CESM2	all major natural and anthropogenic forcings, including original CMIP6 biomass burning aerosols	coupled	as above; used as prior for PDA	50 (first 7 used for PDA)
TPACE	CESM2	as in CESM2-LEcmip6	coupled; nudged to observed SST anomalies (ERSSTv5) in tropical Pacific	sync the model to evolution of observed internal variability in the tropical Pacific	10
CESM2-LE*	CESM2	members of CESM2-LEcmip6 with same initialization years as TPACE	coupled	baseline to isolate effect of nudging in TPACE	10
CESM2-GOGA	CESM2	as in CESM2-LEcmip6; GOGA = 'Global Ocean – Global Atmosphere'	prescribed from ERSSTv5; HadISST1 & OISSTv2 sea ice	find global atmospheric response to observed SST and sea ice anomalies globally	10
CESM2-TOGA	CESM2	as in CESM2-LEcmip6; TOGA = 'Tropical Ocean – Global Atmosphere'	as in GOGA but using climatology polewards of ~28ºN and ~28ºS	find global atmospheric response to observed SST and sea ice anomalies in the tropics and subtropics	10
CESM2-WNUDGE	CESM2	as in CESM2-LEcmip6; winds nudged to ERA5 55ºS-80ºS, above 850 hPa	coupled	constrain model to observed Antarctic winds	1
piControl	CESM2	pre-Industrial control; forcings fixed at nominal 1850 values	coupled	evaluate climate system behavior in the absence of anthropogenic forcing; calculate baseline Antarctic snow accumulation rate	1
CESM1-LE	CESM1	Large Ensemble; all major natural and anthropogenic forcings (CMIP5)	coupled	baseline for comparison to meltwater experiment and as a prior for PDA	40
CESM1-AIS meltwater	CESM1	as in CESM1-LE plus Antarctic meltwater hosing	coupled	find atmosphere-ocean response to freshwater fluxes from Antarctica	10
CESM1-LME	CESM1	time-varying Last Millenium (LM) forcings (850 AD - 1849 AD) with water isotope-enabled CESM1	coupled	as a prior for PDA with minimal influence on spatial covariance from anthropogenic forcings	1

Table 1: Summary of global CESM experiments evaluated in this study. ***Bolded italicized*** experiments have been used in Paleoclimate Data Assimilation (PDA) by *O'Connor et al.* (18) and this study. References and data access links given in *SI Appendix*, Table S1. All CESM2 experiments follow SSP3.7 radiative forcing after 2014; the CESM1 experiments follow RCP8.5 after 2005.

Cumulative AIS mass gain or loss due to snow accumulation

From the MT19 reconstruction, we find a cumulative mass gain over the grounded AIS of 3824 Gt, or 10.5 mm SLE, over the 20th Century (Fig. 1*A,B*), in agreement with the 10.6 mm previously reported (1). The cumulative mass gain arises because the relative mass (i.e., the annual accumulation rate in Gt/y, averaged over the grounded AIS, relative to its 19th Century mean) increases in a stepwise fashion during the 20th Century (*SI Appendix*, Fig. S1*A*). For 1901-1925, the relative mass anomaly is about 20 Gt/y; for 1976-2000 it is above 60 Gt/y. The cumulative mass timeseries is highly correlated with global-mean temperature anomalies in the CESM1-LE PDA (r = 0.92; Fig. 1*E*,*F*). Since MT19 and the PDA share some common proxy data, we check this relationship with the independent SAT dataset from ERA-20C (39), which similarly shows a high correlation with cumulative mass (r = 0.83). Cumulative mass and global temperature anomalies are also highly correlated in CESM2 (r = 0.83 for [TPACE]), where brackets indicate the ensemble mean (hereafter, the same convention is used for all experiments listed in Table 1). This provides the first evidence that the cumulative mass gain is forced, since the global-mean temperature in an ensemble mean is, by definition, the forced response to GHGs and the other radiative forcings imposed in each ensemble member of the experiment.

On the continental scale, both the reconstructions and the model experiments indicate a significant positive correlation between AIS-wide temperature anomalies and relative mass timeseries (*SI Appendix*, Fig. S1*B*), consistent with previous work on the sensitivity of snow accumulation to temperature (40-42). Broadly, these results affirm the thermodynamic expectation of more AIS snow accumulation with warming (5, 41). However, the exact sensitivity varies considerably depending on the choice of averaging period, specific experiment, and/or whether an ensemble mean or individual ensemble member is used. Thus, the global- or Antarctic-mean temperatures do not constrain the magnitude of the snow accumulation increase and are not diagnostic of the physical factors that are driving it. To understand these factors, we evaluate the suite of ensembles listed in Table 1.

[CESM2-LE] indicates a mass gain of 6079 Gt (16.8 mm SLE), well above the MT19 reconstruction. This indicates a large, externally forced accumulation increase. This number is only slightly higher (< 1mm SLE) in the other half of the CESM2-LE (the absence of square brackets refers to the Large Ensemble generally), [CESM2-LEcmip6] (Fig. 1*C,D*). As seen in box-whisker plots (Fig. 1*B,D*), both halves of the CESM2-LE exhibit a large ensemble spread. The 5% lower bound of the CESM2-LE lies within the +1 σ error of MT19, while two outlier ensemble members are within MT19's -1 σ error. Interpreting the CESM2-LE at face value, the reconstructed cumulative mass gain arises from an externally forced response counteracted by an internally driven mass loss of around - 2300 Gt (- 6.4 mm SLE).

Mass accumulated over century-length segments of the piControl suggests that internal variability, in the absence of external forcing, cannot account for the observed mass gain (Fig. 1*B*). Yet, as the ensemble spreads show, it is large enough to partially counteract the forced response in [CESM2-LE] or [CESM2-LEcmip6], and bring model results in agreement with MT19. The TPACE experiment attempts to constrain the evolution of internal variability in the model by nudging it towards observed SST anomalies in tropical Pacific. At 4167 Gt (11.5 mm SLE), mass gain in [TPACE] is only 1 mm greater than MT19 and within its 1 σ error (Fig. 1*B*). The observed variability captured in TPACE reduced 20th-Century cumulative mass by 2312 Gt (6.4 mm SLE), nearly matching the estimate of internal variability in the CESM2-LE that is required to explain the observations (Fig. 1 *C, D*.)

The single-forcing ensembles uncover the two major components of the forced response (Fig. 1 *B,D*). Greenhouse gasses are the dominant driver of the cumulative mass gain, with [GHG] giving a value of 7483 Gt (21 mm SLE), which is twice the value from the reconstruction. Aerosols offset this; mass change in [AAER] is -9 mm SLE. The sum of [GHG] and [AAER], 12 mm SLE, is within the +1 σ error of MT19 (Fig. 1*B*). The other forced responses are comparatively small, at 745 Gt for [EE] and -281 Gt for [BMB]. The sum of the four separate ensemble means is near the top of the +1 σ error range of MT19. Non-linear responses to the forcings, especially aerosols, could explain why [CESM2-LE] is larger than the sum of the separate ensemble means (29). If we suppose that the forced responses combine linearly, the reconstructed value could be interpreted as the combined response to all these forcings, without a significant offsetting role for internal variability.

The results so far, while showing general consistency between the CESM2 and the MT19 reconstruction, suggest two interpretations for the cumulative mass gain in MT19. Namely, the single-forcing ensembles suggest that the 10.5 mm SLE from MT19 is only due to external forcing, with large, opposing responses to GHGs and aerosols. In contrast, both the CESM2-LE and TPACE experiments suggest a smaller role for aerosols, but a large role for internal variability in counteracting the mass gain due to GHGs. We therefore turn to the spatial patterns of snow accumulation and atmospheric circulation change to help inform the most likely interpretation of the trends.

Spatial patterns of snow accumulation and the role of atmospheric circulation

To examine the spatial trend patterns of accumulation, we compute pattern correlations between the 20th-Century trend in MT19 and each ensemble member of the CESM2-LE and TPACE experiments, along with the ensemble means of all CESM2 experiments (*SI Appendix*, Figs. S2-S5). Similarly, pattern correlations for the sea level pressure (SLP) trend across 40ºS-90ºS are computed with the same model experiments and using the CESM2-LE PDA as the observational benchmark. We select the ensemble member whose trend patterns in snow accumulation and atmospheric circulation exhibit the best pattern correlations to the MT19 and PDA reconstructions, respectively. The best-matching individual ensemble member (member 40) comes from CESM2-LEcmip6 (*SI Appendix*, Figs. S2, S3).

Like the reconstructed patterns (Fig. 2*A*), member 40 (Fig. 2*B*) exhibits an accumulation trend dipole across the West Antarctic Ice Sheet (WAIS), consistent with a deepened Amundsen Sea Low (ASL) and stronger onshore onto the eastern WAIS and offshore flow off the western WAIS. On a larger scale, both member 40 and the reconstruction features a pressure dipole between the middle and high southern latitudes, consistent with the strengthening and poleward shift of the westerlies. The reconstructed circulation pattern is more zonally asymmetric than in member 40, which helps to explain the disagreement in accumulation trend patterns across East Antarctica. The ASL deepening trend and strengthening winds in the Pacific sector are robust across many versions of PDA with different model experiments as priors (18, 43), while the poleward shift of the circumpolar westerlies depends on having strong anthropogenic forcing in the prior (18).

Although member 40 has the highest spatial pattern correlations, it exhibits a relatively large cumulative mass gain, just above the inter-quartile range of the ensemble (Fig. 1*D*). Conversely, the ensemble member with the lowest cumulative mass gain, member 20 (Fig. 1*D*), exhibits poor spatial pattern correlations to the reconstructions (*SI Appendix*, Figs. S2, S4). In other words, the extreme case of internal variability in the CESM2-LE that can reconcile the modeled with the reconstructed cumulative mass gain does not manifest in the correct spatial pattern. We find a similar situation with the TPACE experiment. [TPACE] is more poorly correlated with patterns in MT19 and the PDA than [CESM2-LE] and [CESM2-LEcmip6] (*SI Appendix*, Figs. S4, S5.) This discrepancy is explained by the anticyclonic trend over the South Pacific in [TPACE] (Fig. 3*A*, 3B), which is a dynamic response to the SST trend in the tropics (Fig. 3*B*), which can roughly be described as El-Niño like. However, when the full observed global SST field is prescribed in CESM2, as in the CESM2-GOGA ensemble, the ASL deepens (*SI Appendix*, Fig. S6*B*), consistent with the PDA and the spatial trend pattern in accumulation. This La Niña-like teleconnection could arise from the muted warming in the central tropical Pacific (Fig. 3*C*), which, when ENSO variance is removed from the SST data, becomes a cooling trend (44). Since the full global SST field is prescribed, the exact role of the tropical Pacific cannot be inferred from CESM2-GOGA. Results from [TPACE] suggest that tropical Pacific SSTs alone have not driven the ASL deepening and the associated snow accumulation pattern. This is consistent with previous work (45) finding a lack of significant 20th-Century-trends in ENSO or its low-frequency counterpart, the Interdecadal Pacific Oscillation, that could drive ASL deepening. Warming in the western Pacific, east of Australia, may play a role (45); this warming is not simulated by [TPACE].

In the ensemble means, [GHG] and [EE] are best correlated with the reconstructed patterns, exhibiting higher correlations than [TPACE] (*SI Appendix*, Figs. S2, S3). [AAER] has a pattern correlation of -0.57 in SLP and -0.38 for SMB. This suggests that GHGs and the forcings in EE are fully consistent with the spatial-temporal history of snow accumulation and the associated circulation trend, but that aerosols are not. Although aerosols cause a general cooling (Fig. 3*E*), consistent with reduced snow accumulation, they do not explain the spatial patterns in snow accumulation and high-latitude atmospheric circulation. Thus, neither of the two preliminary interpretations mentioned above – that aerosols or an extreme case of internal variability have counteracted the forced response to GHGs (and “everything else” to a lesser extent) – fully fit the data.

To be more explicit, member 40 is separated into its forced (*SI Appendix*, Fig. S7*C*) and internal (*SI Appendix*, Fig. S7*D*) components. This illustrates that the overall increase in accumulation rate is explained by external forcing, while its spatial pattern is more strongly shaped by internal variability. The forced atmospheric circulation pattern indicates a strengthening and poleward shift of the westerlies, especially in the Indian Ocean sector and Drake Passage. In the forced pattern, snow accumulation increases nearly everywhere on the continent, but is especially enhanced on the coasts of the WAIS and QML. The internally driven circulation pattern bears a general resemblance to the forced pattern, but its centers of action are shifted northeastwards. On a broader scale, this internal pattern is associated with cool, La Niña - like SST anomalies in the eastern Pacific (*SI Appendix*, Fig. S6*M,N*). Thus, the La Niña-like SST trend in member 40 helps to explain the atmospheric circulation and snow accumulation trend patterns, but it is not of sufficient magnitude to substantially reduce the forced cumulative mass gain. The limited ability of La Niña to explain the modeled and observed accumulation histories is confirmed by compositing analysis (*SI Appendix*, Fig. S8*A,B,C*).

Next, we quantify the role of the strengthening westerlies by constructing indices of near-surface zonal wind anomalies averaged over 50ºS-70ºS, and calculating the portion of the SLP and accumulation time series at each grid point that are linearly congruent with the trend in the zonal wind indices. The associated patterns in the reconstructions (Fig.*2C*) and member 40 (Fig. 2*D*) are qualitatively similar, with both having a deep ASL and accumulation trend dipole across the WAIS. However, the deeper ASL is more northeastward in the reconstruction, creating a larger area of negative accumulation anomalies on the WAIS, which contributes to a more negative AIS-wide accumulation anomaly than in the free-running model. When the anomalies linearly congruent with the trends in the wind indices are removed from the accumulation timeseries, the MT19 and modeled accumulation rate trends become more consistent with each other, with residual trends of + 110 Gt/y for MT19 (*SI Appendix*, Fig. S7*G*) and +139 Gt/y for member 40 (*SI Appendix*, Fig. S7H). Still, there remains a gap between what reconstructed accumulation trends would have been without the strong wind trend and the trend in member 40, in which the wind trend makes little difference in the AIS-wide accumulation trend.

Role of SST trends and the missing influence of Antarctic meltwater

We suggest that reconstructed winds explain a more negative snow accumulation trend than modeled winds because the former are accompanied by a persistent surface cooling trend, most pronounced in the Pacific Sector of the Southern Ocean (Fig. 4*C*; Fig. 3*I*). We use the PDAs with the CESM1 model priors to represent this trend to avoid the possibility that the reconstructed SAT trend patterns are contaminated by uncertain CMIP6 aerosol and biomass burning forcing. For the mid 20th Century, the reconstructed SAT trend in CESM1-LE PDA (Fig. 4*C,J*) is similar to ERSSTv5 (46) trends (Fig. 4*B*). [CESM2-LEcmip6] does not show cooling (Fig. 4*A*). The CESM2-GOGA ensemble (with prescribed SSTs from ERSSTv5), simulates a sharp decrease in snow accumulation across the WAIS (Fig. 4*F*), consistent with the trend in MT19 (Fig. 4*G*). In this way, GOGA provides evidence that the SST trends are important for the snow accumulation trend, independently of the PDA revealing that the snow accumulation trend on the WAIS is accompanied by cooling in the adjacent south Pacific Ocean.

To unravel the reasons for the trends evident in [CESM2-GOGA] and the reconstructions, we adopt a global perspective (Fig. 1*E*; Fig. 3). The CESM1-LE and CESM1-LM PDAs exhibit reasonable global-mean temperature timeseries (Fig. 1*E*). Their warming of ~ 0.55 °C over the 20th Century (1976:2000 minus 1901:1925) is close to the ~ 0.6 °C from comprehensive land-ocean datasets like HadCRUT5 (47) and GISTEMP (48). Under GHGs alone, late 20th Century warming would have been larger than observed, as shown by the [GHG] timeseries in comparison with the CESM1 PDA reconstructions. Knowing that CESM1 produces the same GHG-driven warming as CESM2 (29), the departure of reconstructed warming from GHG-driven warming is found by subtracting the CESM1-LME PDA from the [GHG] timeseries. This timeseries peaks around 1940, then declines until 2000. In contrast, the CESM2-LE PDA warming trend closely follows that of [GHG] after the 1940s, implying no offset from GHG-driven warming. The CESM2-LE PDA apparently disregards information from aerosols, another indication that CMIP6 aerosol forcing does not fit well with the spatial-temporal evolution of SAT recorded in the proxy data.

The SST trend in ERSSTv5 contains a large patch of muted warming in the southcentral Pacific, from the equator at ~ 150ºW to the eastern Ross Sea region (Fig. 3*C*), where there is an absolute cooling trend in other datasets like ERSSTv3b (*SI Appendix*, Fig. S6A). If the global-mean trend is subtracted from each gridpoint, much of the south Pacific is covered by relative cooling, and so is the entire coastal region of Antarctica (Fig. *3D*). This relative cooling does not appear in [CESM2-LEcmip6] or member 40 (*SI Appendix*, Fig. S6 *F,N*). In fact, the CESM2 has nearly the opposite pattern, with relative south Pacific warming, due to the strong aerosol-driven cooling in the North Pacific (Fig. 3*E*) and the lack of anthropogenic aerosols in the Southern Hemisphere (SH). [TPACE] partially fixes this problem by delivering some cooling to the SH via an atmospheric teleconnection (Fig. 3*A*).

Spatially, the departure from GHG-driven warming can be represented by subtracting surface temperature trends in [GHG] from the same in the CESM1-LME PDA. By design of the PDA, this pattern fits the proxy data, including the variability of snow accumulation. For completeness, [EE] is also subtracted from the PDA-reconstructed field. We name this pattern the Antarctic-Central Pacific Cooling (ACPC) pattern after its spatial structure (Fig. 3*G*). Some combination of aerosols, internal variability, and any missing forcings such as meltwater explains this pattern. Indeed, over the SH oceans (0° to 65°S), the ACPC and [AAER] exhibit a pattern correlation of r = 0.78. However, aerosols cannot explain some of the details evident in the reconstructions, such as the concentration of cooling in the southeastern Pacific, or the deepening of the ASL. Whereas the ACPC emphasizes cooling signals in the SH, the aerosol pattern (Fig. 3*E*) emphasizes the NH, due to the NH sources of industrial aerosol emissions.

From published work with CESM1 and other models, we recognize that ACPC resembles global responses to cooling in the high-latitude SH, imposed in idealized model experiments by reducing incoming shortwave radiation (49) or by prescribing surface heat fluxes (38). These experiments elucidate the atmospheric mechanisms by which SH cooling signals propagate to the tropical Pacific: Anomalously cold, dry polar air is advected by the atmospheric circulation northeastwards towards South America. The anomalous cooling strengthens the mid-latitude jet, deepens the ASL and strengthens the subtropical high, in part due to blocking by the Andes. The stronger subtropical high advects the cold air further equatorward, eventually reaching the subtropics, where shortwave cloud feedbacks, the wind-evaporation-SST feedback, and enhanced coastal upwelling reinforce the cooling. This cooling signal can be advected to the equatorial Pacific by the northeasterly trade winds, where strong atmosphere-ocean coupling triggers the Bjerknes feedback, enhancing eastern equatorial upwelling in a La Niña-like response. The La Niña-like SST pattern drives Rossby wave trains back towards the south Pacific, further deepening the ASL. This explains why La Niña patterns within the CESM2-LE, like in member 40, best fit the reconstructed accumulation and atmospheric circulation patterns. However, the CESM2-LE lacks the initiation of the cooling in the SH. Prescribed negative heat fluxes in the tropics deliver weak cooling to the SO (38), supporting our results that La Niña-like variability is not strong enough to substantially cool the Southern Ocean and reduce snow accumulation.

More realistic, fully coupled experiments illustrate a possible origin for the ACPC. Experiments that include prescribed Antarctic meltwater fluxes (34) and/or wind nudging (34, 50) improve the fit of modeled and observed SST trend patterns (15, 34, 38, 50). We use the meltwater-induced pattern from the CESM1 meltwater hosing ensemble. Over the SH oceans (0° to 65°S), the meltwater-induced pattern (Fig. 3*H*) has a pattern correlation of r = 0.80 with ACPC. When combined with radiative forcing, meltwater produces a snow accumulation trend pattern similar to the trend in [CESM2-GOGA] (Fig. 4 *F,H*). Meltwater is the only forcing that induces strong cooling along the Antarctic coast (Fig. 3 *H*), similar to the observed pattern (Fig. 3*D*). We are not suggesting that ACPC is purely a meltwater-driven pattern, but that meltwater contributes to it and might have triggered it.

On its own, the historical meltwater forcing is not strong enough to cool the eastern and central equatorial Pacific (Fig. 3*H*). This lack of tropical response might be attributable to model biases, such as the double Intertropical Convergence Zone (ITCZ) and/or weak shortwave cloud feedbacks in CESM1 (38, 49). Stronger meltwater forcing in future forcing scenarios (RCP8.5) overcomes these biases, causing a cooling in the equatorial central and eastern Pacific (38). Alternatively, aerosol forcing might be responsible for the cooling trend in this region (Fig. 3*E*; 51). In combination with [GHG] and [EE], the historical meltwater signal is associated with central and eastern equatorial Pacific warming (Fig. 3*J*). In contrast, combining ACPC with [GHG] and [EE] yields muted warming in the equatorial Pacific (Fig. 3*I*), consistent with observations (Fig. 3*C*), and consistent with the pattern correlations suggesting a role for aerosols in the ACPC. Both meltwater and aerosol forcing are uncertain, and future work is required to disentangle their relative roles.

The evidence presented supports a storyline by which Antarctic meltwater reduces Antarctic snow accumulation via its effects on SSTs and atmospheric circulation. In the early 20th Century, rising GHG concentrations, a pause in major volcanic activity, and an increase in solar insolation (29) drove polar-amplified warming (*SI Appendix*, Fig. S6*D,G,H,P*) and a cumulative mass gain consistent with GHGs (Fig. 1*A*). This warming trend was at times amplified by internal variability, most notably the El Niño event of 1939-41 (52). Although the timing of this El Niño is coincident with the onset of modern-day retreat of Pine Island and Thwaites glaciers (53, 54), its causal role in retreat has not been determined. Nonetheless, evidence from marine sediments traces the modern-day thinning (and eventually unpinning) of ice shelves fronting the Pine Island and Thwaites glaciers to the 1940s or early 1950s, which led to grounding line retreat and an increasing freshwater flux from the AIS (54). The onset of retreat also coincides with the timing of ASL deepening (Fig. 4*I*), and cooling in the south Pacific at ~ 150°W (Fig. 4*J*), both of which began in the mid 20th Century, before other potentially significant influences on the ASL, such as stratospheric ozone depletion (28, 43). Additionally, from the mid-20th Century onwards, both GHGs alone and the combined response to all forcings in CESM2-LE overpredict the cumulative mass gain (Fig. 1*A*), suggesting the existence of a damping factor. Observed SST trends since the 1940s are consistent with the damping of GHG-driven warming (55). The main mechanism is stabilizing shortwave cloud feedbacks in the tropics and SH subtropics (34, 49, 51, 55), which can be activated by Antarctic meltwater (34) and aerosols (51).

In the Southern Ocean, meltwater causes increased stratification and a reduction in the ocean-atmosphere heat flux, especially in the Pacific sector where the underlying circumpolar deepwater is on or close to the continental shelf. Reduced heat flux in this region drives the ACPC pattern in SST and SLP, by the mechanisms in the idealized experiments discussed above. Moreover, the location of the cold surface anomaly reconstructed by PDA (Fig. 4*C*) agrees with the location of strongest SST cooling in response to meltwater hosing (Fig 4*D*). During the late 20th Century and early 21st Century, the observed acceleration of AIS mass loss (3, 4) implies that the influence of meltwater has increased. This is consistent with ERSSTv5, which shows cold anomalies at 150°W, 60°S have persisted and strengthened through 2022 (*SI Appendix*, Fig. S8*D*).

The 21st Century

Snow accumulation trend patterns over 2001-2022, as given by ERA5 (*SI Appendix*, Fig. S9*A*) and the CESM2 experiment nudged to ERA5 winds (*SI Appendix*, Fig. S9*B*), are qualitatively similar to those of the 20th Century. An underlying increase due to rising GHGs and stratospheric ozone depletion (31) is evident in the forced response (Fig. 2*E*). Wind anomalies deliver opposing patterns of positive and negative accumulation trends across both the WAIS and East Antarctica (Fig. 2*F*), masking the forced response, but not causing a reduction in Antarctic-wide snow accumulation. Consistent with results from the reconstructions, the CESM2-WNUDGE results show that atmospheric circulation trends have not been the major factor in counteracting the warming-driven snow accumulation increase. Rather, the forced response is likely over-estimated because of the SST pattern effect, in which the CESM2-LE does not simulate observed SST trends.

As support for this idea, [CESM2-GOGA] shows no AIS-wide trend over 1980-2013, in contrast to ~4% accumulation rate increases in [CESM2-LEcmip6] and [TPACE] (*SI Appendix*, Fig. S10A), relative to their late-20th Century means. These results are in concert with the well-observed south Pacific cooling and expansion of sea ice in the eastern Ross Sea, and help explain the results from regional modeling studies, which have shown no significant Antarctic-wide trend since 1980 (11, 12). Prescribing observed SST trends in CESM2, whether in the tropics or globally, helps to explain both the spatial pattern and magnitude of trends in snow accumulation. Remarkably, if the coupled model is constrained only by Antarctic meltwater fluxes but no other observed trends, it produces less than a 1% increase in the accumulation rate, and a similar spatial pattern ($r = 0.62$) to [CESM2-GOGA]. The Antarctic snow accumulation trend is consistent with a meltwater signal in observed SST trends.

We have shown that SST trends matter for historical snow accumulation trends on the AIS. To project future changes in snow accumulation and their effect on sea level, there is little constraint on how SST trends might evolve. Since cumulative mass gain is the metric that matters for sea level, and [GHG] + [AAER] approximates the cumulative mass gain over the 20th Century, we use [GHG] + [AAER] to make a rough projection to 2050 (*SI Appendix*, Fig. S11). About 30 mm of sea level mitigation from increased snow accumulation is possible over 2001-

2050. Although measurable, this trend is unlikely to keep pace with dynamic mass loss, especially if meltwater continues to cool SSTs. The future of Southern Ocean SSTs can be viewed as a competition between meltwater effects and an eventual strong warming as ocean heat uptake becomes less effective (16). How this competition plays out will determine the future of snow accumulation on the AIS. We have added evidence in support of the idea that the evolution of tropical Pacific SSTs and in turn the many downstream climate impacts driven by tropical Pacific SSTs, depends on the trajectory of Southern Ocean SSTs (15, 16, 38, 56), with roles for wind and various feedbacks in propagating the signal to the tropics (38, 49).

Discussion and conclusion

In summary, we interpret the 20th Century history of Antarctic snow accumulation using a suite of single-forcing and all-forcing large ensembles from the CESM2, evaluating what factors explain the historical trends, and therefore may be applied towards more accurate projections of snow accumulation into the future. As demonstrated by ice-core based reconstructions (1, 2) and modern satellite observations (4, 57), increased snow accumulation has the power to partially mitigate the contribution on the AIS to sea level rise. Our first-order result is that GHGs have been the major driver of increased snow accumulation on the AIS, leading to a cumulative mass gain of 21 mm SLE on their own, due to their role in warming the atmosphere and ocean surface. The combination of natural forcings and changes in ozone concentrations in the "everything else" ensemble leads to a much smaller mass gain. Internal variability over the 20th Century does not explain a significant cumulative mass gain.

The model's GHG-driven increase overpredicts the MT19 cumulative mass gain by a factor of two. According to the all-forcings CESM2-LE, this overprediction could be reconciled by an extreme pattern of internal variability, or according to the single-forcing simulations, by assuming a very large offsetting role for anthropogenic aerosols. With context from PDA reconstructions, we offer a more likely explanation: The model's overprediction of cumulative mass gain is due to an SST pattern that is not resolved and does not originate in the tropics. In contrast to the model, the PDA and observed SST datasets show a pattern of cooling in the south Pacific Ocean that commenced in the mid-20th Century. The impact of this cooling pattern on snow accumulation is corroborated by a prescribed SST experiment. Other model experiments identify the SST pattern, ACPC, as likely driven by Antarctic meltwater, while independent geologic evidence for when major Antarctic ice shelves and glaciers started retreating fits the timing of when this pattern first emerges. For the 1980-2013 period directly covered by the CESM1 meltwater hosing experiment, the accumulation trend associated with meltwater is similar to that obtained from experiments in which observed SSTs and sea ice concentrations are prescribed. Our results explain the lack of an Antarctic-wide snow accumulation increase since ~1980, which has not been previously attributed.

As additional context for our interpretation, we note that CMIP6 aerosol forcing is problematic (26, 30, 36), while several studies find that extreme internal variability is not a likely explanation for observed SST trends (3, 4, 54, 55, 56). By extension, neither aerosol forcing nor extreme variability are satisfactory explanations for Antarctic accumulation trends. We also highlight strengthening westerly winds (18) as a main driver of snow accumulation trend patterns. However, unlike SSTs, winds mainly act to redistribute snow accumulation and do not lead to a substantial net gain or loss, consistent with previous findings (11). In comparison with satellite data, accumulation trend patterns in [CESM2-GOGA] and [CESM1-AIS meltwater] (*SI Appendix*, Fig. S10*A*) are similar to the pattern of AIS mass change derived from satellite laser altimetry (57). The prominent forced mass gain in QML (Fig. 2*E*), counteracted by mass loss in Wilkes Land (Fig. 2*F*), is remarkably similar to the pattern of AIS mass change inferred from satellite gravity data (4).

Given the importance of snow accumulation as a player in sea level rise, and as a recorder of globally relevant SST patterns, we urge expanded modeling and observational efforts focused on Antarctic snow accumulation and meltwater. The CESM2 has several shortcomings; it is low resolution, it lacks important surface processes like blowing snow, and most importantly, it lacks coupling between the AIS and the ocean. Sensitivity to meltwater hosing varies widely across climate models, and the magnitude of meltwater-induced anomalies shown here may not be realistic (43). Also, the available meltwater experiment does not isolate the role of meltwater from the Pine Island and Thwaites glaciers. To enable more targeted experiments and to test sensitivities across different models, expanded observational estimates of historical meltwater fluxes are needed, ideally covering the entire 20th Century, and seamlessly integrated into future forcing scenarios. The ice core network used in reconstructions like MT19 and the PDAs has not been extended. Broader ice core coverage would give more confidence in trends in coastal areas and the interior of East Antarctica. Despite these limitations, we have documented a notable fidelity of the CESM in simulating the trend patterns observed by satellites and ice cores. To gain confidence in model-based projections, this agreement should be further explored and quantified.

Materials and Methods

Snow accumulation reconstruction, CESM2 and cumulative mass calculation

The dataset of annual snow accumulation is described in *Medley and Thomas* (1). It was calibrated to the spatial signature of precipitation minus evaporation (*P minus E*) in the MERRA-2 atmospheric reanalysis (S1), with a bias correction based on accepted *in-situ* measurements. We specifically use the version regridded by *Dunmire et al*. (6) from its native 1° resolution to the standard grid of CESM2's land and atmosphere components. The grounded AIS is as defined by *Zwally et al.* (S2). Unlike ref. (1), we do not include Antarctic islands in our calculation of Antarctic-wide snow accumulation. For Antarctic-wide snow accumulation, grid-cell values in mm w.e. yr^{-1} are scaled by the area of the respective grid cell, and summed over the grounded AIS for each year of the dataset. This mass timeseries is converted to a relative mass timeseries by subtracting the long-term mean for 1801-1900 (1927.4 Gt/yr) from the entire timeseries. Cumulative mass is calculated by integrating the relative mass timeseries with time, starting in 1901. The sea level equivalence at the year 2000 is obtained by dividing the cumulative mass by 361 Gt/mm. This procedure was repeated for +1 $\boldsymbol{\sigma}$ and -1 $\boldsymbol{\sigma}$ error timeseries; the gridded standard error fields are as provided by ref. 1.

The Community Earth System Model, version 2 (CESM2) is a comprehensive model with coupled land, atmosphere, sea ice and ocean components, as fully described in ref. (25). All experiments evaluated here (Table 1) use the standard 1° horizontal resolution. References and data sources for the experiments are given in *SI Appendix*, Table S1.

From CESM2 output, we estimate net annual snow accumulation to be comparable with the reconstruction. From the land model component, SNOW and RAIN variables are used as the precipitation terms, while QSOIL and QRUNOFF are used as the ablation terms. Monthly data are summed to annual means by weighting each monthly value by the length of the month, using the same weighting for each year, as there are no leap years in CESM2 output. The relative and cumulative mass timeseries are determined by the same method as for the MT19 reconstruction, except for the calculation of the baseline value, which is described below. This procedure is performed for each ensemble member of each experiment. The SLE numbers quoted in the text have been rounded to the nearest half mm.

Crucial for the calculation of cumulative mass timeseries and sea level equivalence from CESM2 is the estimate of the baseline accumulation rate that is representative of nineteenth-century values in a stable climate. We iterated with a few different approaches, including referencing each ensemble member to its own nineteenth-century value using the years 1850-1900 as the reference period. This proved to be too affected by interannual to decadal variability. We settled on using the same reference value from the piControl simulation for all ensemble members of all experiments. With this approach, responses to 20th-Century radiative forcing are more detectable. We used the value over the 452-year period, years 1000-1451 of the piControl. The value is 2012.9 Gt/yr. It is important to recognize that all ensemble members of all historical experiments (except for CESM2-WNUDGE and CESM2-GOGA) evaluated here were initialized within this piControl segment, between the years 1001 and 1301, which was chosen because it is relatively stable (25, 29, 30). An ensemble member initialized from the piControl year 1301 at calendar year 1850 would reach calendar year 2000 150 years later, overlapping with the piControl through year 1451. This overlap method is a way of ensuring that mass accumulated by year 2000 arises from forcing (or internal variability), minimizing the influence of drift.

For the CESM2-GOGA ensemble, we did not find a representative base period from a long, uncoupled control integration. Biases in coupled CESM2 SSTs (25) and uncertain nineteenth century observed SSTs (46) further complicate the use of CESM2-GOGA. We therefore use CESM2-GOGA only to evaluate spatial patterns of change over selected time periods, and not for cumulative mass timeseries. The same considerations apply to CESM2-TOGA.

Wind-nudged experiment

The CESM2-WNUDGE simulation is forced with CMIP6 historical forcing through 2014 and thereafter with SSP3.7 forcing. It is initialized from a CESM2-LEcmip6 ensemble member in 1950 and zonal (U) and meridional (V) winds over 1950-present are nudged to 6-hourly ERA5 U and V from 850 hPa to the top of the model between 55ºS and 80ºS following previously described methodology (20, S3). The first few decades of CESM2-WNUDGE show signs of drift in the Antarctic accumulation values; we therefore use only the 21st Century portion of this experiment.

Deriving Forced vs internal components and responses due to tropics, wind nudging or meltwater

The forced response is defined as the ensemble-mean of all ensemble members of a given experiment. It indicates the model's response to external radiative forcings (greenhouse gasses, aerosols, etc.) imposed in the experiment. By definition, each individual ensemble member has the same forced response. The internal component of a given ensemble member is found by removing the forced response from that member.

We use a similar approach to isolating the role of the tropical SST nudging in the TPACE experiment, meltwater in the CESM1-AIS meltwater experiment, and Antarctic wind nudging in CESM2-WNUDGE. Namely, ensemble means are subtracted from each other. For example, to isolate the effect of nudging to observed tropical SST anomalies in TPACE, [CESM2-LEcmip6] is subtracted from [TPACE]. In this instance, we used only the 10 members of the CESM2-LE that had the same initialization states in the piControl as the 10 members of TPACE. This yields the precise role of tropical SSTs, which is necessary for the cumulative mass gain calculation. The procedure for finding the SST anomalies due to Antarctic meltwater hosing, by subtracting the forced response in CESM1-LE, is described in *Dong et al*. (38). For the anomalies due to wind nudging, we used the forced response as given by all 50 members of CESM2-LEcmip6.

PDA Reconstruction with CESM2-LEcmip6 prior and ASL Index

We generate a PDA reconstruction following the methodology by *O'Connor et al.* (18) with an updated PDA prior formed using the first seven members of CESM2-LEcmip6. The global proxy network is the same as in ref. (18); it includes Antarctic ice core data used in the MT19 reconstruction. The PDA uses the framework developed by *Hakim et al.* (S4), which is an offline ensemble Kalman filter approach. We also extend the PDA reconstructions using the CESM1-LE prior and the CESM1 LME prior published by ref. 18 back to 1850, so all PDA reconstructions are available from 1850 to 2005. The reconstructions show good agreement with the ERA5 reanalysis in the key focus regions of this study, including the circumpolar wind belt region, the Amundsen Sea Low region, and the tropical Pacific (*SI Appendix*, Fig. S12). The reconstructions are in anomalies relative to 1961 to 1990 unless otherwise noted. As in ref. (18), the ASL Index is the standardized mean SLP over 60°-75°S, 180°-310°E.

Pattern correlations and wind-congruent trends

Pattern correlations are the Pearson correlation coefficient of the linear correlation between two maps of the same variable. Before computing this statistic, any necessary regridding and/or masking is performed, and the lat-lon arrays are collapsed into a single vector. We use the uncentered (no mean value removed) pattern correlation of the trend fields.

We estimate the wind-congruent accumulation and SLP trends first by representing the standardized wind index timeseries (computed for both the reconstruction and ensemble member 40) and the accumulation and SLP fields at each grid point as anomalies relative to 1901-2000. All timeseries, including the wind indices and the accumulation and SLP fields at each grid point are then linearly detrended. Then, the linear regression coefficient is calculated between the detrended accumulation or SLP fields and the detrended wind timeseries. These regression coefficients are multiplied by the 1901-2000 trend in the wind index to give the wind-congruent trends in accumulation or SLP. Residual trends are found by subtracting the wind-congruent trends from the original anomaly fields, and then calculating the linear trends of the residual fields.

DATA AND CODE AVAILABILITY

Output from all CESM2 experiments used here is on the Glade file system at the National Science Foundation – National Center for Atmospheric Research (NSF NCAR), and nearly all experiments are publicly accessible as listed in (*SI Appendix*, Table S1). Table S2 lists the sources of the observational datasets discussed here, including MT19 and the PDA reconstructions. The code for generating the snow accumulation timeseries and maps in the main figures will be available on Github upon acceptance of the manuscript.

ACKNOWLEDGEMENTS

DPS, ZY, ZIC, and RTD were supported by the US National Science Foundation (NSF) Office of Polar Programs (OPP) grant #1952199. ZY received additional support from NSF HDR iHARP grant #2118285. DPS received additional support from the NSF NCAR, which is a major facility sponsored by the NSF, under cooperative agreement no. 1852977. GKO was supported by the Washington Research Foundation postdoctoral fellowship. EBW received support from NSF OPP grant #2213988. ZIC received additional support from the NSF-sponsored Significant Opportunities for Atmospheric Research and Science (SOARS) program. ZE was supported by the U.S. Department of Energy, Office of Science, Office of Advanced Scientific Computing Research, Department of Energy Computational Science Graduate Fellowship under Award Number(s) DE-SC0023112. This report was prepared as an account of work sponsored by an agency of the United States Government. Neither the United States Government nor any agency thereof, nor any of their employees, makes any warranty, express or implied, or assumes any legal liability or responsibility for the accuracy, completeness, or usefulness of any information, apparatus, product, or process disclosed, or represents that its use would not infringe privately owned rights. Reference herein to any specific commercial product, process, or service by trade name, trademark, manufacturer, or otherwise does not necessarily constitute or imply its endorsement, recommendation, or favoring by the United States Government or any agency thereof. The views and opinions of authors expressed herein do not necessarily state or reflect those of the United States Government or any agency thereof. The authors thank all the scientists, software engineers, and administrators who contributed to the development of CESM, which is primarily supported by the NSF. The Climate Variability and Change Working Group led the production of the CESM2 Large Ensemble, and the CESM2-

GOGA, TPACE, and the single-forcing ensembles. The authors appreciate Jan T.M. Lenaerts for collaboration in obtaining funding, and Yue Dong and Andrew Pauling for providing data from the CESM1 meltwater hosing experiment. The authors thank Yue Dong, Jan T.M. Lenaerts and Eric J. Steig for insightful discussions that helped improve this work.

AUTHOR CONTRIBUTIONS

DPS designed the study, obtained primary funding, and led the writing of the paper. ZY, DPS, and GKO created analysis code and figures. GKO led the PDA reconstructions. EBW and ZE led the wind-nudged experiment. ZIC and RTD contributed to analysis and interpretation. DPS, ZY, EBW and RTD mentored students involved in the project. All authors reviewed the paper.

REFERENCES

1. B. Medley, E. R. Thomas, Increased snowfall over the Antarctic Ice Sheet mitigated twentieth-century sea-level rise. *Nature Clim Change* **9**, 34–39 (2018).

2. Y. Wang, C. Xiao, An Increase in the Antarctic Surface Mass Balance during the Past Three Centuries, Dampening Global Sea Level Rise. *Journal of Climate* **36**, 8127–8138 (2023).

3. E. Rignot, et al., Four decades of Antarctic Ice Sheet mass balance from 1979–2017. *Proc. Natl. Acad. Sci. U.S.A.* **116**, 1095–1103 (2019).

4. I. Velicogna, et al., Continuity of Ice Sheet Mass Loss in Greenland and Antarctica From the GRACE and GRACE Follow-On Missions. *Geophysical Research Letters* **47** (2020).

5. B. Fox-Kemper et. al., Ocean, Cryosphere and Sea Level Change, in *Climate Change 2021: The Physical Science Basis. Contribution of Working Group I to the Sixth Assessment Report of the Intergovernmental Panel on Climate Change* [V. Masson-Delmotte et al., eds], 1211-1362 (2021).

6. D. Dunmire, J. T. M. Lenaerts, R. T. Datta, T. Gorte, Antarctic surface climate and surface mass balance in the Community Earth System Model version 2 during the satellite era and into the future (1979–2100). *The Cryosphere* **16**, 4163–4184 (2022).

7. C. Palerme, et al., Evaluation of current and projected Antarctic precipitation in CMIP5 models. *Clim Dyn* **48**, 225–239 (2016).

8. R. Winkelmann, A. Levermann, M. A. Martin, K. Frieler, Increased future ice discharge from Antarctica owing to higher snowfall. *Nature* **492**, 239–242 (2012).

9. M. E. Jones, et al., Sixty Years of Widespread Warming in the Southern Middle and High Latitudes (1957–2016). *Journal of Climate* **32**, 6875–6898 (2019).

10. J. Turner, T. A. Lachlan-Cope, S. Colwell, G. J. Marshall, W. M. Connolley, Significant Warming of the Antarctic Winter Troposphere. *Science* **311**, 1914–1917 (2006).

11. J. T. M. Lenaerts, B. Medley, M. R. van den Broeke, B. Wouters, Observing and Modeling Ice Sheet Surface Mass Balance. *Reviews of Geophysics* **57**, 376–420 (2019).

12. R. Mottram, et al., What is the surface mass balance of Antarctica? An intercomparison of regional climate model estimates. *The Cryosphere* **15**, 3751–3784 (2021).

13. K. R. Clem, et al., Antarctica and the Southern Ocean. *Bulletin of the American Meteorological Society* **104**, S322–S365 (2023).

14. L. N. Boisvert, et al., Intercomparison of Precipitation Estimates over the Southern Ocean from Atmospheric Reanalyses. *Journal of Climate* **33**, 10627–10651 (2020)

15. K. C. Armour, et al., Sea-surface temperature pattern effects have slowed global warming and biased warming-based constraints on climate sensitivity. *Proc. Natl. Acad. Sci. U.S.A*. **121** (2024).

16. S. M. Kang, et al., Global impacts of recent Southern Ocean cooling. *Proc. Natl. Acad. Sci. U.S.A.* **120** (2023).

17. E. Blanchard-Wrigglesworth, L. A. Roach, A. Donohoe, Q. Ding, Impact of Winds and Southern Ocean SSTs on Antarctic Sea Ice Trends and Variability. *Journal of Climate* **34**, 949–965 (2021).

18. G. K. O'Connor, E. J. Steig, G. J. Hakim, Strengthening Southern Hemisphere Westerlies and Amundsen Sea Low Deepening Over the 20th Century Revealed by Proxy-Data Assimilation. *Geophysical Research Letters* **48** (2021).

19. M. Previdi, L. M. Polvani, Anthropogenic impact on Antarctic surface mass balance, currently masked by natural variability, to emerge by mid-century. Environ. Res. Lett. **11**, 094001 (2016).

20. E. Blanchard-Wrigglesworth, T. Cox, Z. I. Espinosa, A. Donohoe, The Largest Ever Recorded Heatwave—Characteristics and Attribution of the Antarctic Heatwave of March 2022. *Geophysical Research Letters* **50** (2023).

21. E. R. Thomas, et al., Regional Antarctic snow accumulation over the past 1000 years. *Clim. Past* **13**, 1491–1513 (2017).

22. B. Medley, et al., Temperature and Snowfall in Western Queen Maud Land Increasing Faster Than Climate Model Projections. *Geophysical Research Letters* **45**, 1472–1480 (2018).

23. A. J. Monaghan, et al., Insignificant Change in Antarctic Snowfall Since the International Geophysical Year. *Science* **313**, 827–831 (2006).

24. A. Eswaran, O. J. Truax, T. J. Fudge, 20th-Century Antarctic Sea Level Mitigation Driven by Uncertain East Antarctic Accumulation History. *Geophysical Research Letters* **51** (2024).

25. G. Danabasoglu, et al., The Community Earth System Model Version 2 (CESM2). *J Adv Model Earth Syst* **12** (2020).

26. M. Casado, R. Hébert, D. Faranda, A. Landais, The quandary of detecting the signature of climate change in Antarctica. *Nat. Clim. Chang*. **13**, 1082–1088 (2023).

27. R. C. J. Wills, Y. Dong, C. Proistosecu, K. C. Armour, D. S. Battisti, Systematic Climate Model Biases in the Large-Scale Patterns of Recent Sea-Surface Temperature and Sea-Level Pressure Change. *Geophysical Research Letters* **49** (2022).

28. D. L. Hartmann, The Antarctic ozone hole and the pattern effect on climate sensitivity. *Proc. Natl. Acad. Sci. U.S.A*. **119** (2022).

29. I. R. Simpson, et al., The CESM2 Single-Forcing Large Ensemble and Comparison to CESM1: Implications for Experimental Design. *Journal of Climate* **36**, 5687–5711 (2023).

30. K. B. Rodgers, et al., Ubiquity of human-induced changes in climate variability. *Earth Syst. Dynam.* **12**, 1393–1411 (2021).

31. J. T. M. Lenaerts, J. Fyke, B. Medley, The Signature of Ozone Depletion in Recent Antarctic Precipitation Change: A Study With the Community Earth System Model. *Geophysical Research Letters* **45** (2018).

32. R. Chemke, M. Previdi, M. R. England, L. M. Polvani, Distinguishing the impacts of ozone and ozone-depleting substances on the recent increase in Antarctic surface mass balance. *The Cryosphere* **14**, 4135–4144 (2020).

33. G. A. Schmidt, et al., Anomalous Meltwater From Ice Sheets and Ice Shelves Is a Historical Forcing. *Geophysical Research Letters* **50** (2023).

34. Y. Dong, A. G. Pauling, S. Sadai, K. C. Armour, Antarctic Ice-Sheet Meltwater Reduces Transient Warming and Climate Sensitivity Through the Sea-Surface Temperature Pattern Effect. *Geophysical Research Letters* **49** (2022).

35. D. P. Schneider, J. E. Kay, C. Hannay, Cloud and Surface Albedo Feedbacks Reshape 21st Century Warming in Successive Generations of An Earth System Model. *Geophysical Research Letters* **49** (2022).

36. M. M. Holland, et al., New model ensemble reveals how forcing uncertainty and model structure alter climate simulated across CMIP generations of the Community Earth System Model. *Geosci. Model Dev*. **17**, 1585–1602 (2024).

37. H. Hersbach, et al., The ERA5 global reanalysis. *Quart J Royal Meteoro Soc* **146**, 1999–2049 (2020).

38. Y. Dong, K. C. Armour, D. S. Battisti, E. Blanchard-Wrigglesworth, Two-Way Teleconnections between the Southern Ocean and the Tropical Pacific via a Dynamic Feedback. *Journal of Climate* **35**, 6267–6282 (2022).

39. P. Poli, et al., ERA-20C: An Atmospheric Reanalysis of the Twentieth Century. *Journal of Climate* **29**, 4083–4097 (2016).

40. A. J. Monaghan, D. H. Bromwich, D. P. Schneider, Twentieth century Antarctic air temperature and snowfall simulations by IPCC climate models. *Geophysical Research Letters* **35** (2008).

41. K. Frieler, et al., Consistent evidence of increasing Antarctic accumulation with warming. *Nature Clim Change* 5, 348–352 (2015).

42. Q. Dalaiden, et al., How useful is snow accumulation in reconstructing surface air temperature in Antarctica? A study combining ice core records and climate models. *The Cryosphere* **14**, 1187–1207 (2020).

43. Q. Dalaiden, A. P. Schurer, M. C. Kirchmeier-Young, H. Goosse, G. C. Hegerl, West Antarctic Surface Climate Changes Since the Mid-20th Century Driven by Anthropogenic Forcing. Geophysical Research Letters **49** (2022).

44. S. Lee, et al., On the future zonal contrasts of equatorial Pacific climate: Perspectives from Observations, Simulations, and Theories. *npj Clim Atmos Sci* **5** (2022).

45. P. R. Holland, et al., Anthropogenic and internal drivers of wind changes over the Amundsen Sea, West Antarctica, during the 20th and 21st centuries. *The Cryosphere* **16**, 5085–5105 (2022).

46. B. Huang, et al., Extended Reconstructed Sea Surface Temperature, Version 5 (ERSSTv5): Upgrades, Validations, and Intercomparisons. *Journal of Climate* **30**, 8179–8205 (2017).

47. C. P. Morice, et al., An Updated Assessment of Near-Surface Temperature Change From 1850: The HadCRUT5 Data Set. *JGR Atmospheres* **126** (2021).

48. N. J. L. Lenssen, et al., Improvements in the GISTEMP Uncertainty Model. *JGR Atmospheres* **124**, 6307–6326 (2019).

49. H. Kim, S. M. Kang, J. E. Kay, S.-P. Xie, Subtropical clouds key to Southern Ocean teleconnections to the tropical Pacific. *Proc. Natl. Acad. Sci. U.S.A*. **119** (2022).

50. L. A. Roach, et al., Winds and Meltwater Together Lead to Southern Ocean Surface Cooling and Sea Ice Expansion. *Geophysical Research Letters* **50** (2023).

51. U. K. Heede, A. V. Fedorov, Eastern equatorial Pacific warming delayed by aerosols and thermostat response to CO2 increase. *Nat. Clim. Chang*. **11**, 696–703 (2021).

52. D. P. Schneider, E. J. Steig, Ice cores record significant 1940s Antarctic warmth related to tropical climate variability. *Proc. Natl. Acad. Sci. U.S.A*. **105**, 12154–12158 (2008).

53. J. A. Smith et al., Sub-ice-shelf sediments record history of twentieth-century retreat of Pine Island Glacier. *Nature* **541**, 77–80 (2017).

54. R. W. Clark, et al., Synchronous retreat of Thwaites and Pine Island glaciers in response to external forcings in the presatellite era. *Proc. Natl. Acad. Sci. U.S.A*. **121** (2024).

55. T. Andrews, et al., On the Effect of Historical SST Patterns on Radiative Feedback. *JGR Atmospheres* **127** (2022).

56. S. G. Yeager, et al., Reduced Southern Ocean warming enhances global skill and signal-to-noise in an eddy-resolving decadal prediction system. *npj Clim Atmos Sci* **6** (2023).

57. B. Smith, et al., Pervasive ice sheet mass loss reflects competing ocean and atmosphere processes. *Science* **368**, 1239–1242 (2020).

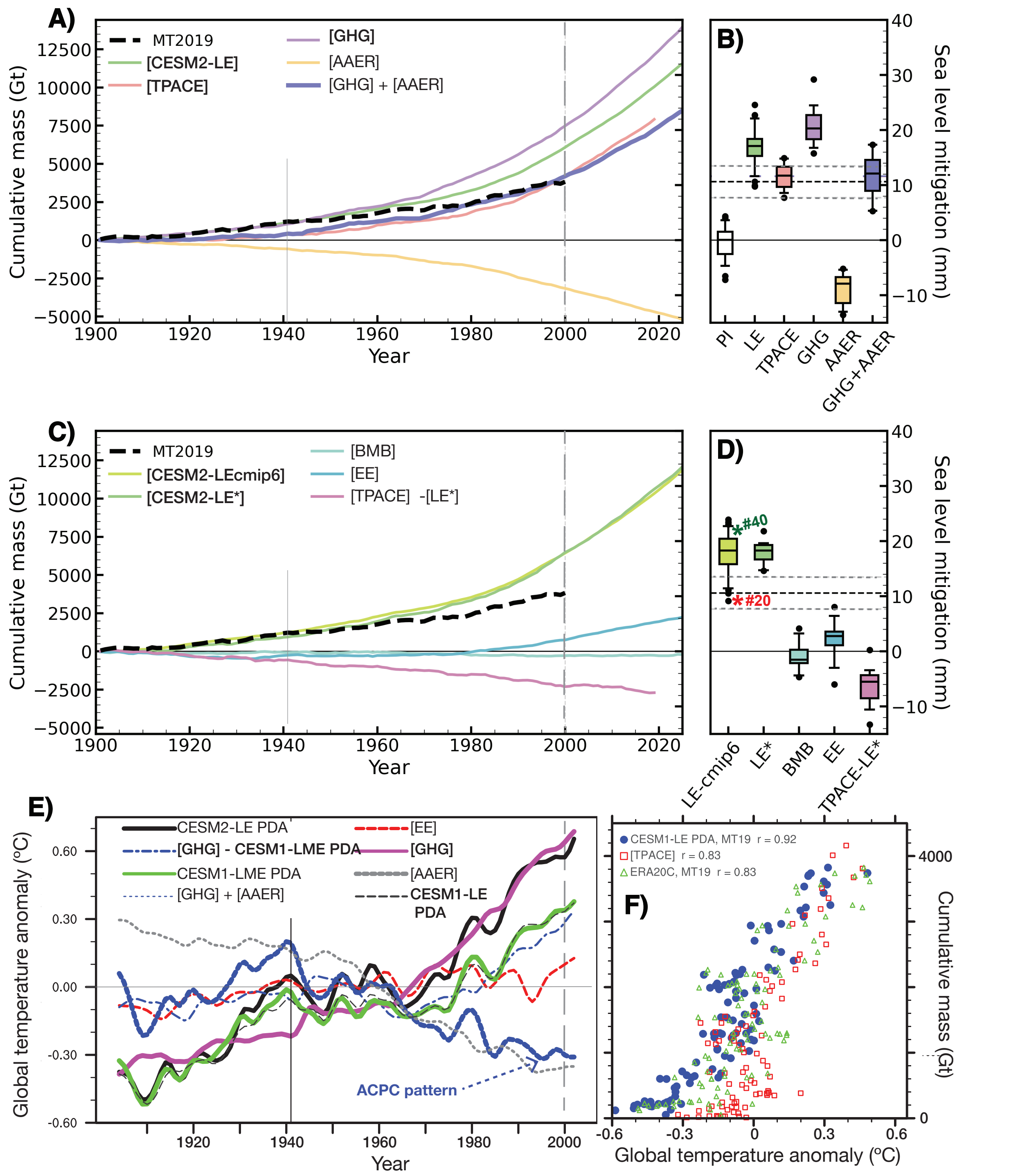

Fig. 1. Cumulative mass and equivalent sea level mitigation due to accumulated snow on the grounded Antarctic Ice Sheet (AIS) in MT19 and CESM2, compared with single-forcing and reconstructed global surface temperature anomalies during the 20[th] Century. ***(A)*** Cumulative mass timeseries from MT19 compared with timeseries from selected ensemble means. ***(B)*** Box plot indicating ensemble spread of cumulative mass at the year 2000 for each of the ensembles and the pseudo ensemble generated by summing 15 individual members of GHG and AAER. The boxes indicate the interquartile range; the median is shown by a horizontal line. Whiskers represent the 5% and 95% bounds of the ensemble, with the values lying outside of these bounds indicated by closed black circles. “PI” refers to the piControl simulation: mass was accumulated over 24 overlapping, 100-year segments. Dashed black horizontal line indicates the mean value of MT19; gray dashed lines indicate +/- 1 sigma errors; ***(C)*** As in a), but for different ensembles and [TPACE] - [CESM2-LE*]. ***(D)*** As in b), but for the ensembles shown in c). Approximate values for members #40 and #20 are indicated by astericks. ***(E)*** Global temperature anomalies in single-forcing ensembles, along with the anomalies in the CESM2-LE PDA, the CESM1-LE PDA, and the CESM1-LME PDA. Also shown is the departure of CESM1-LME PDA from the [GHG] timeseries. All timeseries smoothed with a 7y low-pass filter. ***(F)*** Scatter plot of annual-mean global-mean temperature anomalies versus cumulative mass timeseries over 1901-2000.

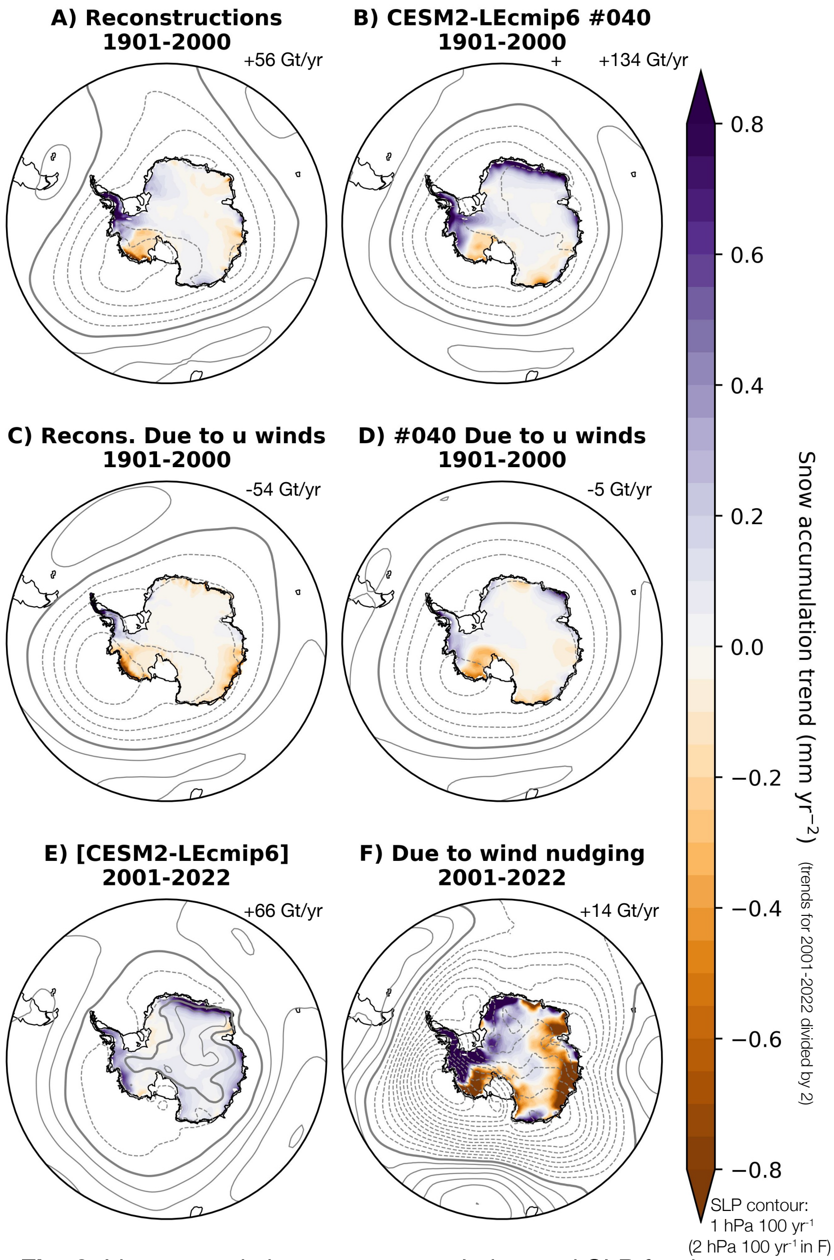

Fig. 2. Linear trends in snow accumulation and SLP for the indicated time periods and model or reconstructed data as discussed in the text. The ***(A)*** 1901-2000 reconstructed trend patterns are best matched by ***(B)*** member #040 of the CESM2-LEcmip6 ensemble. Trend patterns congruent with the trend zonal winds are found for ***(C)*** the reconstructions and ***(D)*** member #40. For the early 21st Century, a ***(E)*** strong forced response is simulated; ***(F)*** results from the wind-nudged experiment indicate that accumlation trends have been strongly shaped by winds, but not offsetting the forced response.

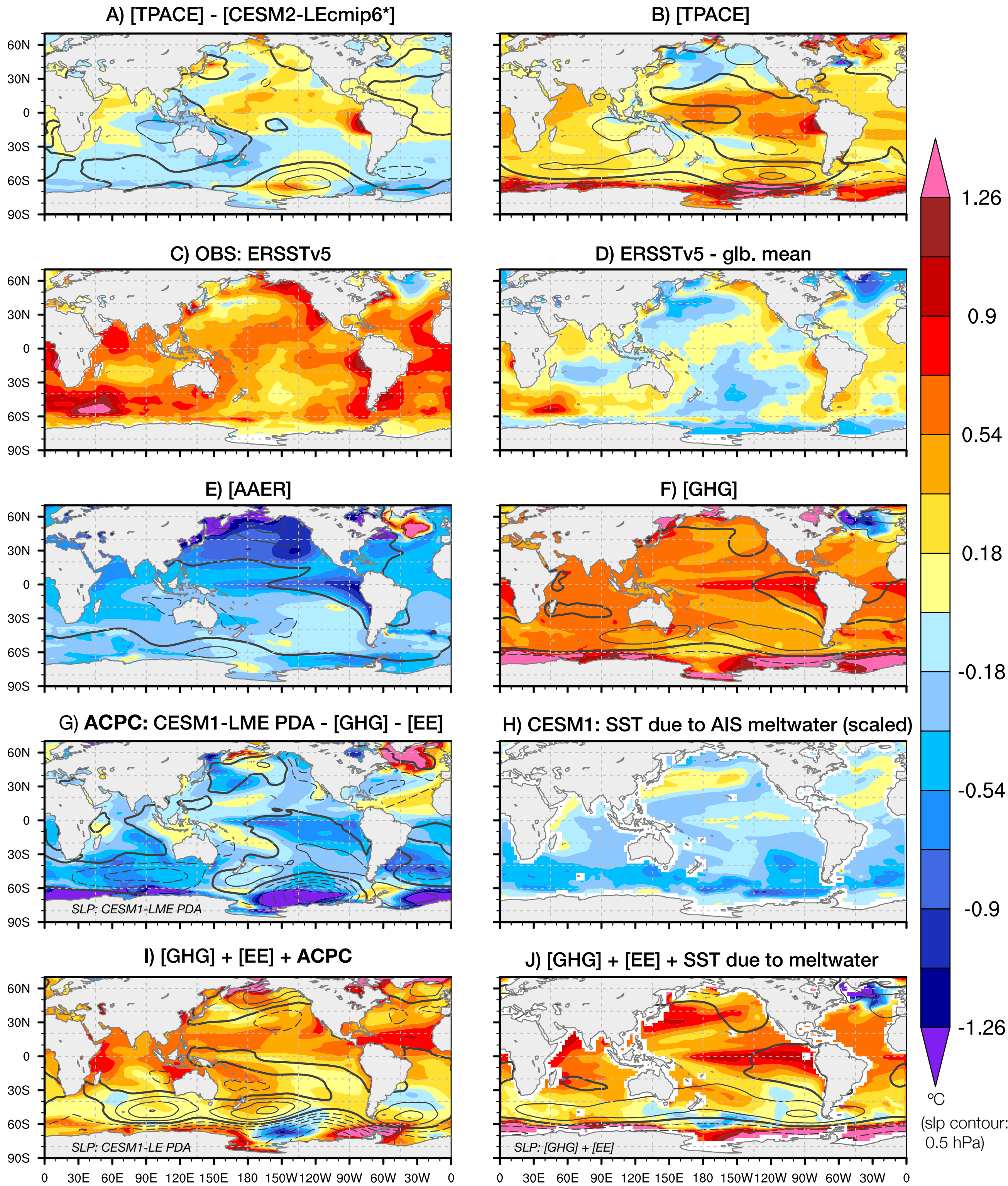

Fig. 3: Surface temperature patterns (1976:2000 minus 1901:1925): ***(A)*** Due to tropical SST nudging in [TPACE]; ***(B)*** [TPACE]; ***(C)*** Observed ERSSTv5 dataset; ***(D)*** ERSSTv5 with global-mean trend removed; ***(E)*** [AAER]; ***(F)*** [GHG]; ***(G)*** Antarctic-Central Pacific Cooling Pattern, ACPC, is found by subtraction of [GHG] and [EE] from the CESM1-LME PDA SAT pattern; ***(H)*** Due to AIS meltwater; this is the trend per decade in the meltwater anomaly from CESM1 historical experiments (33) multiplied by five to estimate meltwater's role over the second half of the century. ***(I, J)*** Approximations of the observed trend pattern (C) are obtained by ***(I)*** adding [GHG] and [EE} to ACPC; ***(J)*** adding the meltwater pattern to [GHG] + [EE]. SLP contours (dashed = negative; sold = positive; zero line bolded) are shown for select plots. Additional maps are in supporting information (*SI Appendix*, Fig. S6)

.

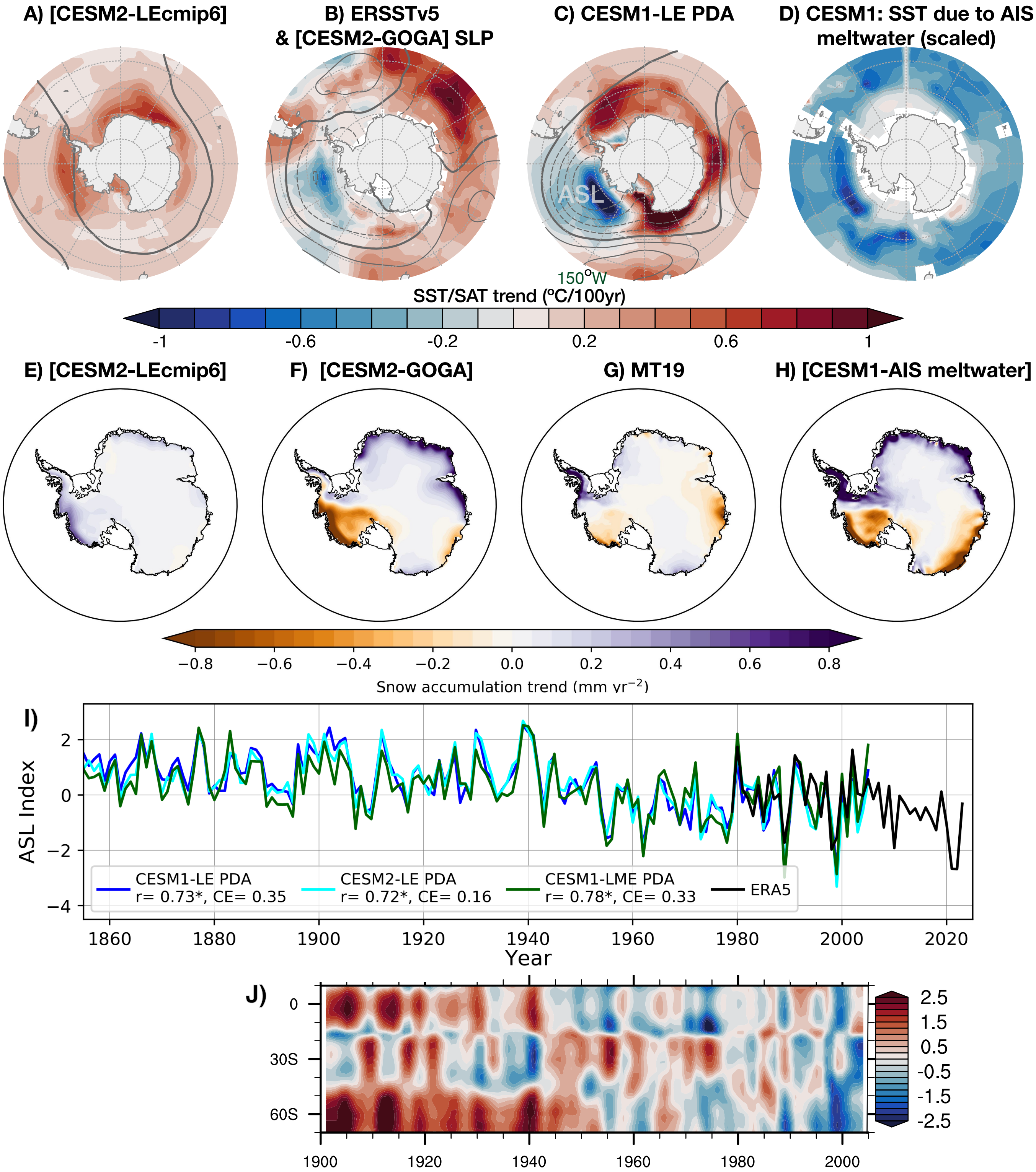

Fig. 4. ***(A-D)*** 1901-1970 trends in ***(A)*** surface temperature and SLP from [CESM2-LEcmip6]; ***(B)*** SST from ERSSTv5 and SLP from [CESM2-GOGA]; ***(C)*** SAT and SLP from CESM1-LE PDA; ***(D)*** SST from the CESM1-AIS meltwater experiment (decadal trend scaled by 3; radiatively forced response removed). ***(E-H)*** Corresponding trend patterns in snow accumulation for ***(E)*** [CESM2-LEcmip6]; (F) [CESM2-GOGA]; ***(G)*** MT19 reonstruction; ***(H)*** [CESM1-AIS meltwater] (1980-2013 trend; radiative forcing included). ***(I)*** Timeseries of ASL index from three different instances of PDA, compared with ERA5. Anomalies relative to 1979-2005. ***(J)*** Timeseries of standardized SAT anomalies (relative to 1979-2005) from CESM1-LME PDA at 150°W. The global-mean timeseries was removed at each gridpoint, and a 3y-lowpass filter was applied.

SUPPLEMENTATY INFORMATION for

Increased Antarctic snowfall mitigates sea level rise less than projected due to meltwater influence on sea surface temperatures

David P. Schneider*[(a,b)]; Ziqi Yin[(c)]; Gemma K O'Connor[(d)]; Edward Blanchard-Wrigglesworth[(e)]; Zaria I. Cast[(f)]; Rajashree Tri Datta[(c)]; Zachary I. Espinosa[(e)]

a. Cooperative Institute for Research in Environmental Sciences, University of Colorado – Boulder, Boulder, CO 80309 USA
b. Climate and Global Dynamics Laboratory, National Center for Atmospheric Research, Boulder, Colorado, 80305 USA
c. Department of Atmospheric and Oceanic Sciences, University of Colorado – Boulder, CO 80309 USA
d. School of Oceanography, University of Washington, Seattle, WA 98195 USA
e. Department of Atmospheric Sciences, University of Washington, Seattle, WA 98195 USA
f. Department of Geography, University of Colorado – Boulder, Boulder, CO 80309 USA

*Corresponding Author: David P. Schneider
email: David.Schneider-1@colorado.edu

Contents of this PDF file:

abbreviation(s)	data availability	main reference(s)
GHG, AAER, BMB, and EE	https://www.cesm.ucar.edu/working-groups/climate/simulations/cesm2-single-forcing-le	29
CESM2-LE and CESM2-LEcmip6	https://www.cesm.ucar.edu/community-projects/lens2	30
TPACE	https://doi.org/10.26024/GTRS-TF57; https://www.cesm.ucar.edu/working-groups/climate/simulations/cesm2-pacific-pacemaker	S5
CESM2-GOGA and CESM2-TOGA	https://www.cesm.ucar.edu/working-groups/climate/simulations/cam6-prescribed-sst	
CESM2-WNUDGE	*forthcoming – selected variables to be published on Zenodo*	S3
CESM1-AIS meltwater	request from original authors (Dr. Yue Dong and Dr. Andrew Pauling)	S6; 38
CESM1-LE	https://www.cesm.ucar.edu/community-projects/lens	S7
CESM2 piControl	https://doi.org/10.22033/ESGF/CMIP6.7733	S8; 25

Table S1. Data availability and main references for the CESM experiments analyzed in this study. Further description in Table 1 of the main text.

abbreviation(s)	data availability	main reference(s)
MT19 snow accumulation	https://earth.gsfc.nasa.gov/cryo/data/antarctic-accumulation-reconstructions	1
CESM1-LE PDA	https://zenodo.org/records/5507607	18
CESM1-LME PDA	https://zenodo.org/records/5507607	18
CESM2-LE PDA	*forthcoming – to be published on Zenodo*	this study
ERSSTv5	https://www.ncei.noaa.gov/products/extended-reconstructed-sst	46
ERSSTv3b	https://www.ncei.noaa.gov/products/extended-reconstructed-sst	S9
ERA5	https://doi.org/10.24381/cds.f17050d7	37
ERA20C	https://doi.org/10.5065/D6VQ30QG	39

Table S2. Data availability and main references for the observational datasets (including reanalysis and reconstructions) used in this study.

SUPPLEMENTAL REFERENCES:

S1. R. Gelaro, et al., The Modern-Era Retrospective Analysis for Research and Applications, Version 2 (MERRA-2). J. Climate 30, 5419–5454 (2017).

S2. Zwally, H. J., Giovinetto, M. B., Beckley, M. A., and Saba, J. L.: Antarctic and Greenland drainage systems, GSFC Cryospheric Sciences Laboratory [data set], http://icesat4.gsfc.nasa.gov/cryo_data/ant_grn_drainage_systems.php (last access: 1 August 2022), 2012.

S3. Espinosa, Zachary, Edward Blanchard-Wrigglesworth, and Cecilia Bitz. "Record Low Antarctic Sea Ice in Austral Winter 2023: Mechanisms and Predictability." Authorea Preprints (2024).

S4. G. J. Hakim, et al., The last millennium climate reanalysis project: Framework and first results. JGR Atmospheres 121, 6745–6764 (2016).

S5. Rosenbloom, Nan, CESM2 Pacific Pacemaker Ensemble. UCAR/NCAR - CISL - CDP. https://doi.org/10.26024/GTRS-TF57. Deposited 2022.

S6. A. G. Pauling, C. M. Bitz, I. J. Smith, P. J. Langhorne, The Response of the Southern Ocean and Antarctic Sea Ice to Freshwater from Ice Shelves in an Earth System Model. Journal of Climate 29, 1655–1672 (2016).

S7. J. E. Kay, et al., The Community Earth System Model (CESM) Large Ensemble Project: A Community Resource for Studying Climate Change in the Presence of Internal Climate Variability. Bulletin of the American Meteorological Society 96, 1333–1349 (2015).

S8. G. Danabasoglu, D. Lawrence, K. Lindsay, W. Lipscomb, G. Strand, NCAR CESM2 model output prepared for CMIP6 CMIP piControl. Earth System Grid Federation. https://doi.org/10.22033/ESGF/CMIP6.7733. Deposited 2019.

S9. User Engagement And Services Branch, Extended Reconstructed Sea Surface Temperature (ERSST) Monthly Analysis, Version 3b. NOAA National Centers for Environmental Information. https://doi.org/10.7289/V5Z31WJ4. Deposited 2010.

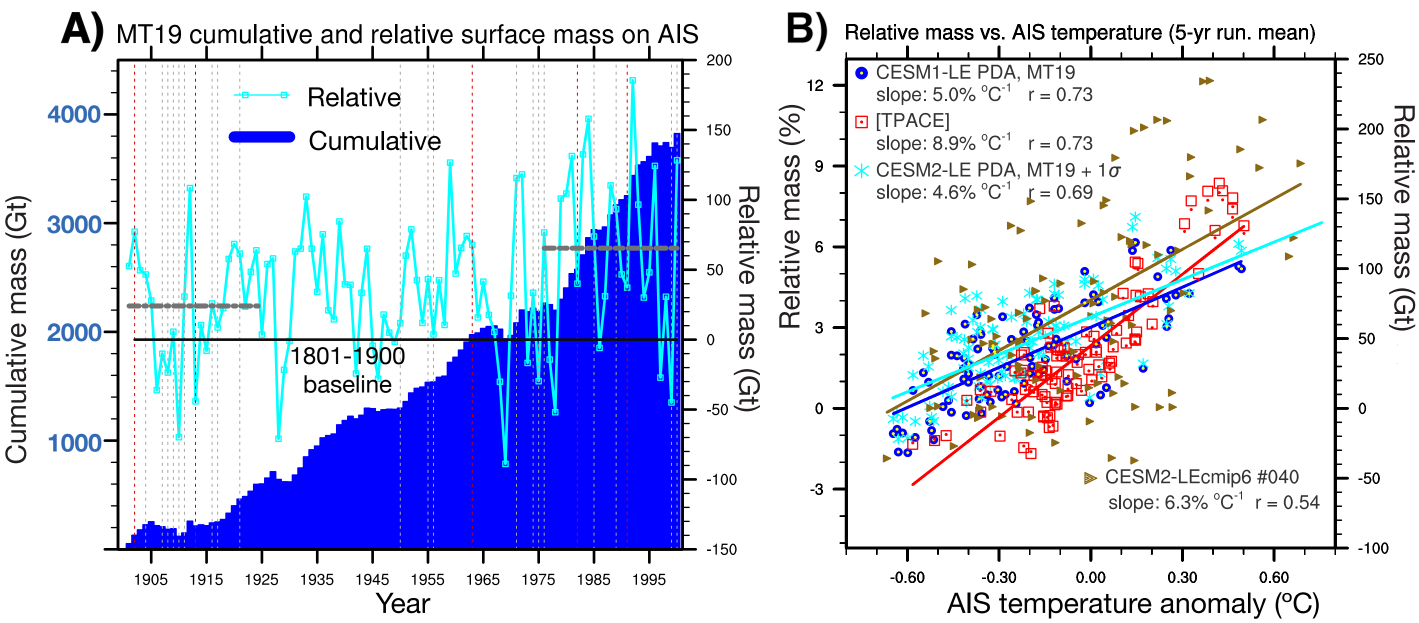

Fig. S1. ***(A)*** Cumulative mass and relative mass timeseries from MT19. Baselines for 1901-1925 and 1976-2000 are indicated as dark gray horizontal lines. La Niña years, used for composites in Fig. S8, indicated by dashed gray vertical lines. Major volcanic eruptions indicated by dashed red vertical lines; ***(B)*** Scatter plot of AIS relative mass versus AIS temperature anomaly, illustrating the temperature-accumulation slope for selected reconstructions and CESM2 experiments. A 5y running mean was applied to the annual-mean timeseries before computing the slopes and correlation values.

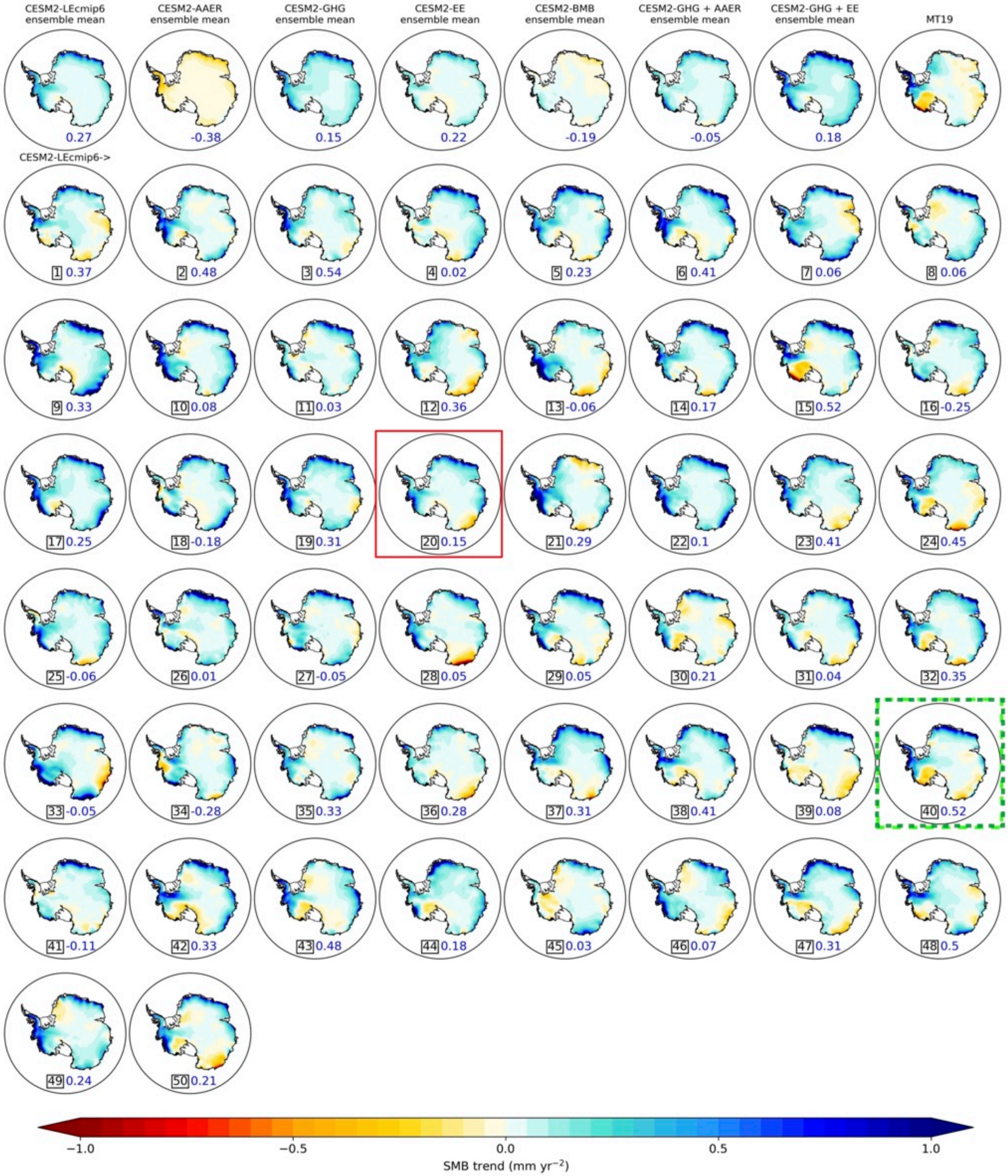

Fig. S2. "Postage stamp" maps displaying the twentieth-century snow accumulation (SMB) trend in [CESM2-LEcmip6], [AAER], [GHG], [EE], and [BMB], along with all 50 ensemble members of the CESM2-LEcmip6. Included in the top row is the trend in the MT19 snow accumulation. At the bottom-center of every model map, the spatial pattern correlation coefficient with MT19 over the grounded AIS is shown. Trends are calculated as epoch differences of 1976:2000 minus 1901:2000 annual means. Member #40 is highlighted with a dashed green square; member #020 is highlighted with a red solid square.

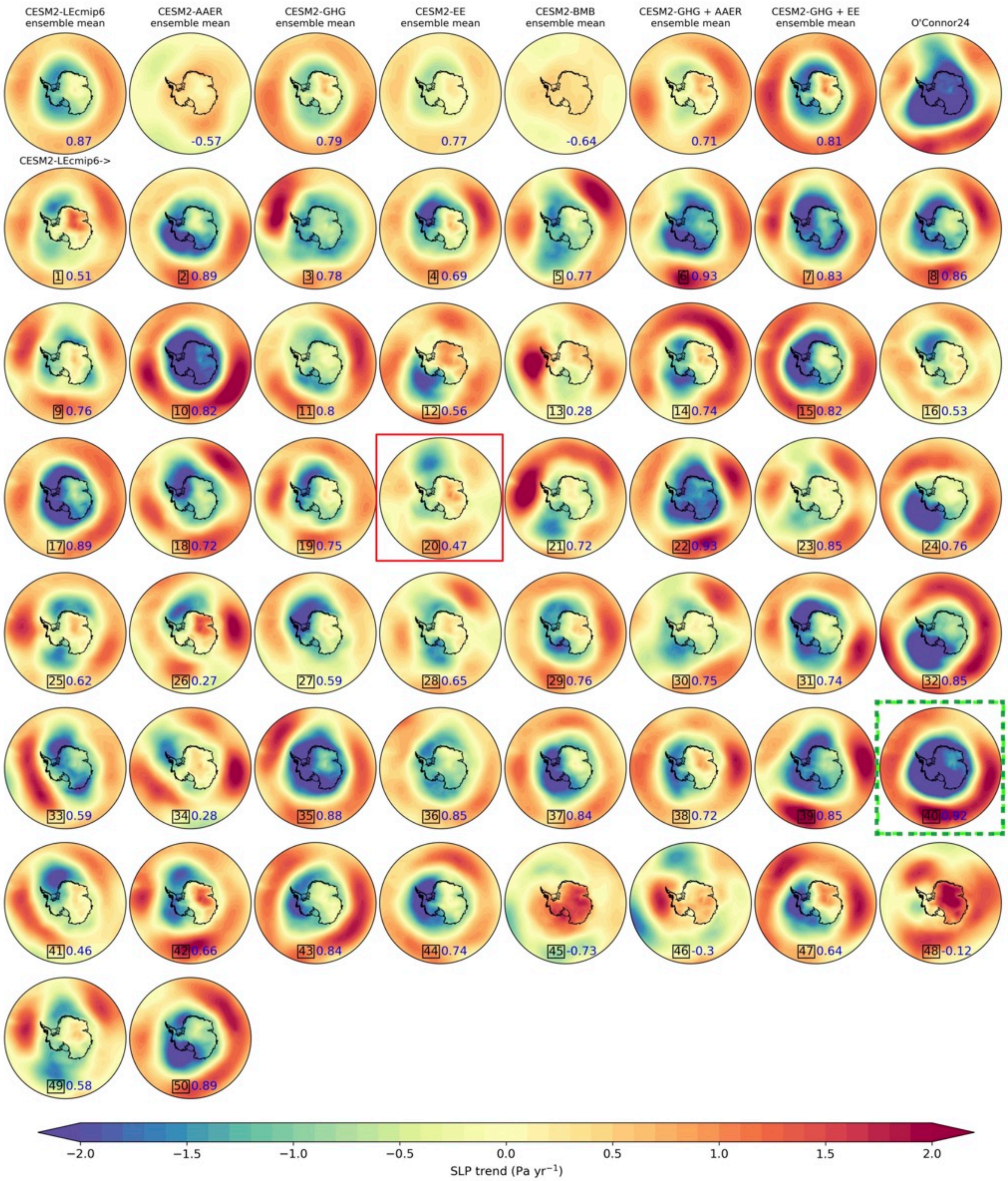

Fig. S3. As in Fig. S2, but for SLP and using the CESM2-LE PDA reconstruction (labeled O'Connor24) as the benchmark for the pattern correlation over 40°S-90°S.

Fig. S4. "Postage stamp" maps displaying the twentieth-century snow accumulation (SMB) trend in [CESM2-LE], [CESM2-LE*], and [TPACE], along with all 50 ensemble members of the CESM2-LE and the 10 members of TPACE. Included in the top row is the trend in the MT19 snow accumulation. At the bottom-center of every model map, the spatial pattern correlation coefficient with MT19 over the grounded AIS is shown. Trends are calculated as epoch differences of 1976:2000 minus 1901:2000 annual means.

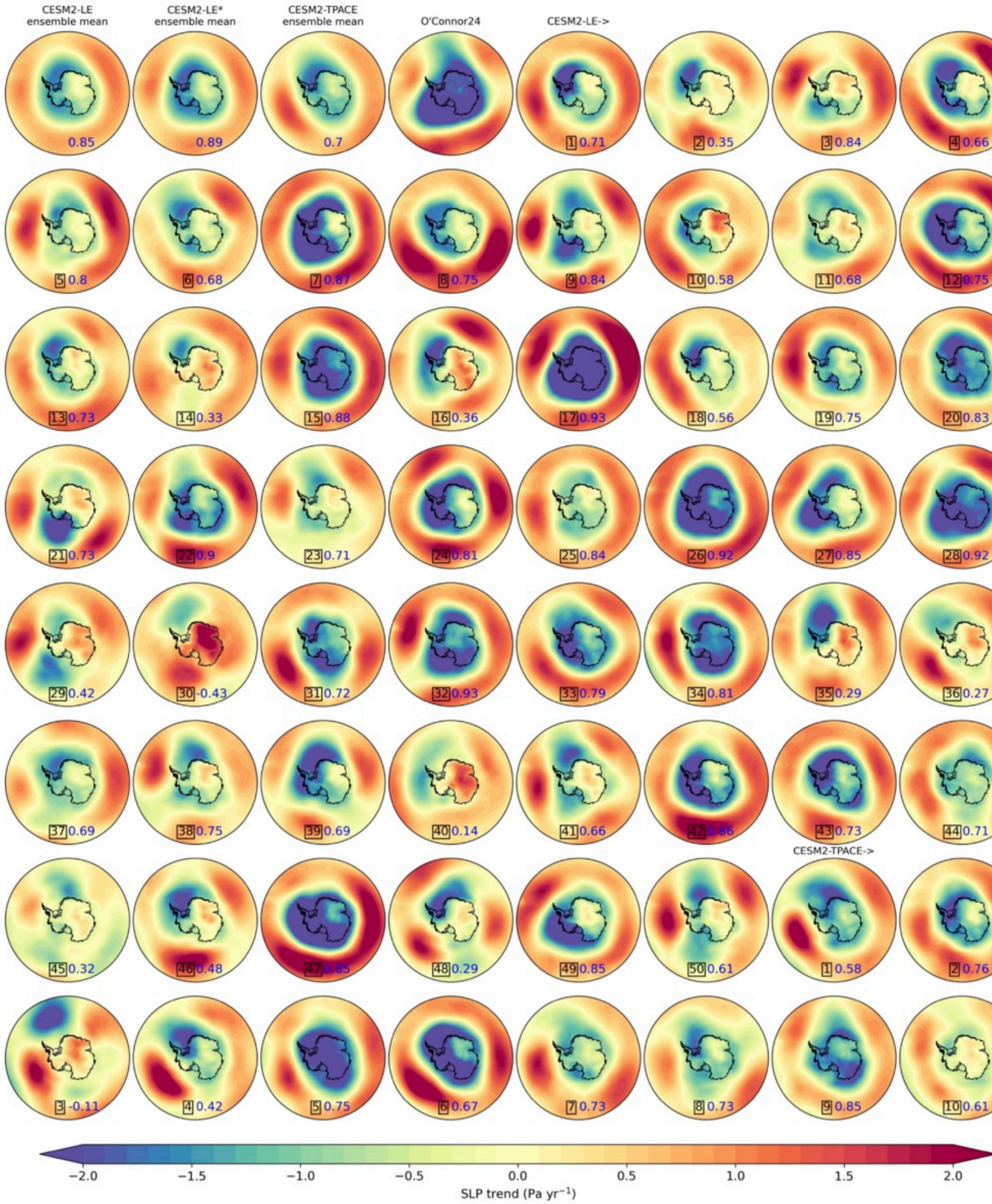

Fig. S5. As in Fig. S4, but for SLP and using the CESM2-LE PDA reconstruction (labeled O'Connor24) as the benchmark for the pattern correlation over 40°S-90°S.

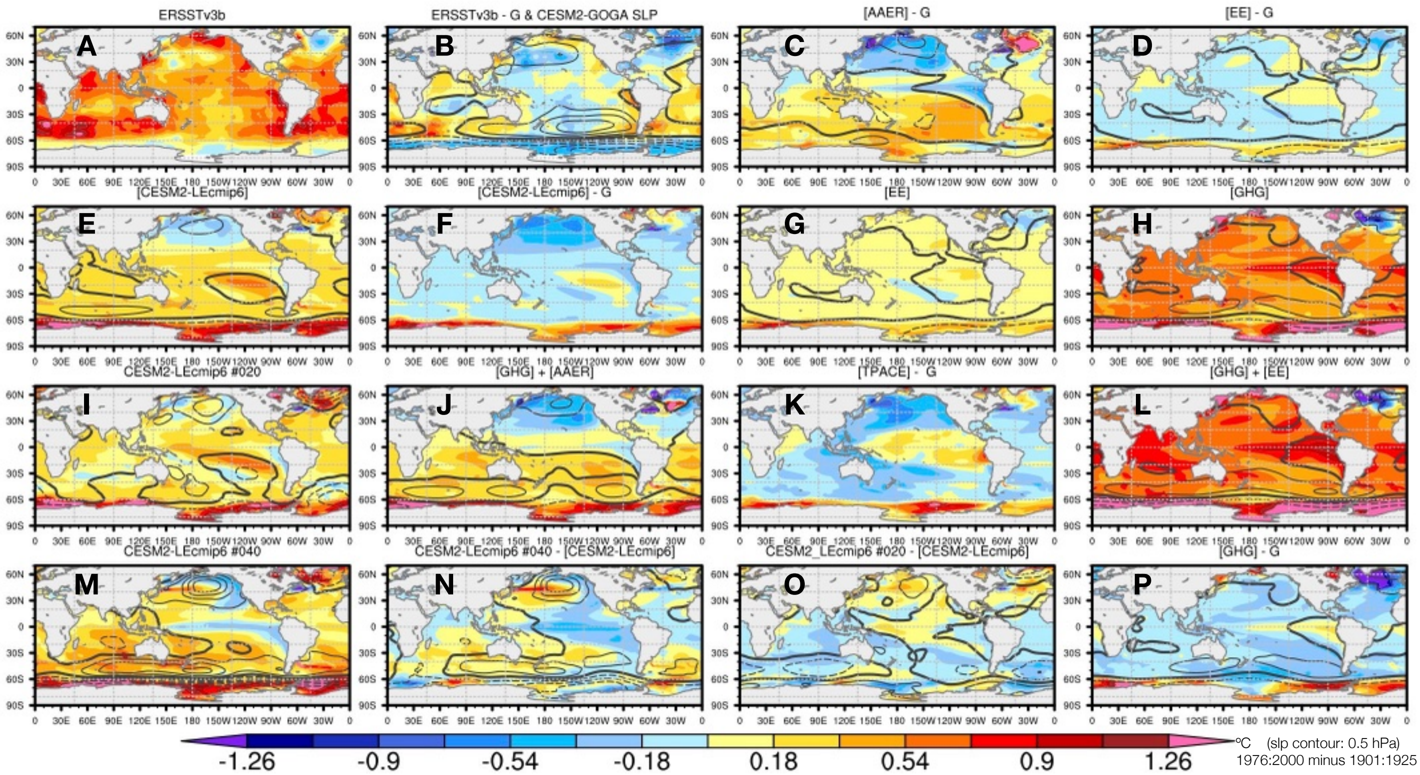

Fig. S6. Extension of Figure 3 from the main text. Surface temperature trend patterns (1976:2000 minus 1901:1925) for ***(A,B)*** observations and ***(C-P)*** various model experiments, as discussed in the text. "G" referes to the global-mean temperature trend, which has been removed from some maps. SLP contours are shown for selected maps (global-mean not removed for SLP).

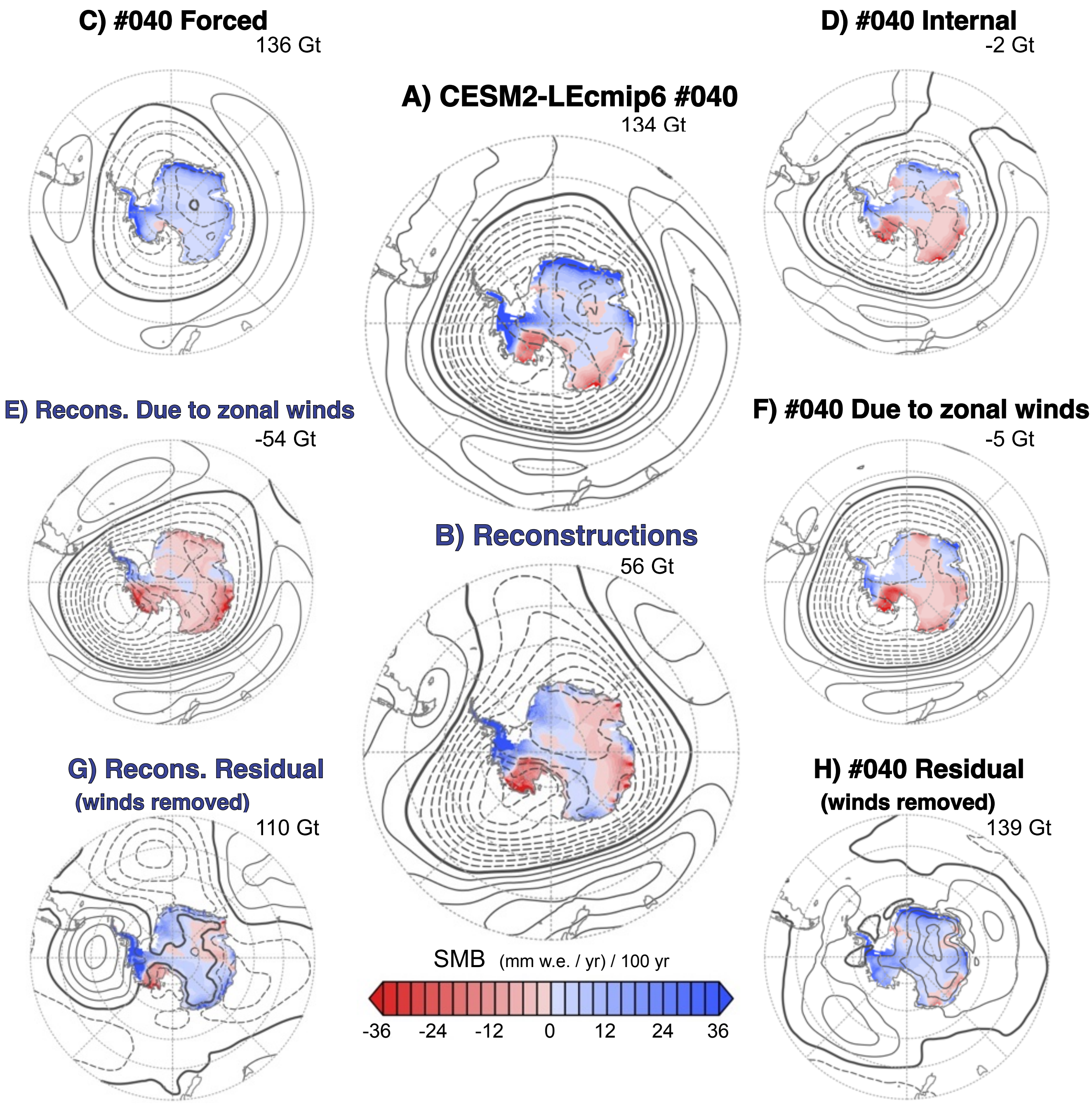

Fig. S7. Extension of Figure 4 from the main text. ***(A)*** Member 40 exhibits the highest pattern correlations to the ***(B)*** reconstructions, and is broken down into its ***(C)*** forced and ***(D)*** internal components. Both the ***(E)*** reconstructed and ***(F)*** modeled snow accumulation have trends that are linearly congruent with trends in the winds. ***(G, H)*** Residual patterns when the wind-congruent trends are removed.

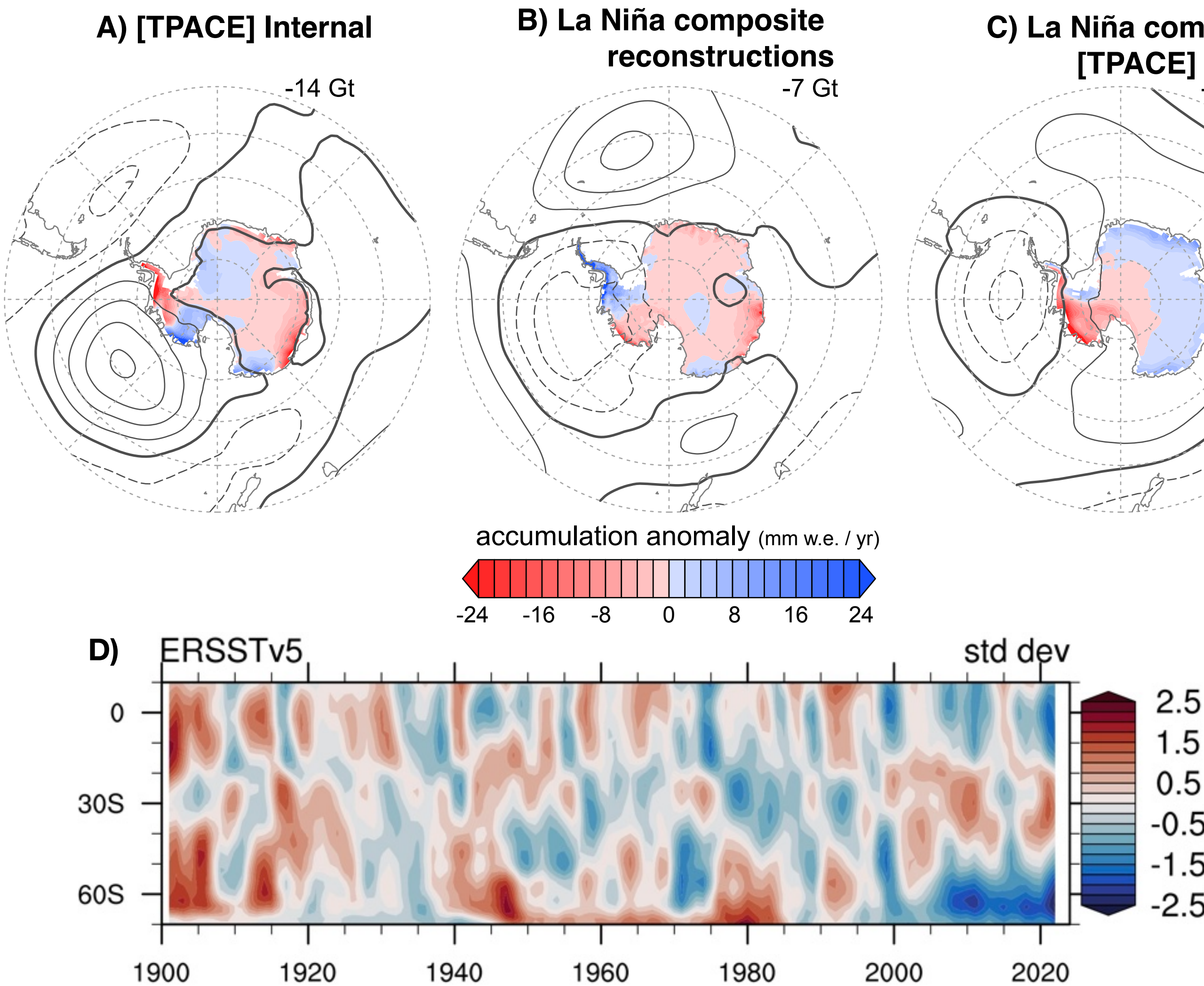

Fig. S8. ***(A)*** Tropically driven ([TPACE] - [CESM2-LEcmip6*]) trend patterns in SLP and snow accumulation (1976:2000 minus 1901:1925), indicating a 14 Gt/y reduction in the AIS-wide accumlation rate despite an El Nino-like circulation pattern. ***(B, C)*** Composites of snow accumulation and SLP anomalies during real La Nina years over 1901-2000. Accumulation and SLP timeseries were lineraly detrended before forming the composites. Although the the reconstructions and TPACE experiment agree on the AIS-wide anomaly of -7 Gt for an average La Nina year, the spatial patterns disagree. La Nina years are defined from NOAA's extended multivariate ENSO index, using austral autumn (MAM) values (https://psl.noaa.gov/enso/climaterisks/years/top24enso.html). The composites are of years 1902, 1904, 1907, 1908, 1909, 1910, 1911, 1913, 1916, 1917, 1921, 1950, 1955, 1956, 1963, 1971, 1974, 1975, 1976, 1982, 1985, 1989, 1991, 1999, and 2000. ***(D)*** Timeseries of standardized SAT anomalies (relative to 1901-2023) from ERSSTv5 at 150ºW. The global-mean timeseries was removed at each gridpoint, and a 3y-lowpass filter was applied.

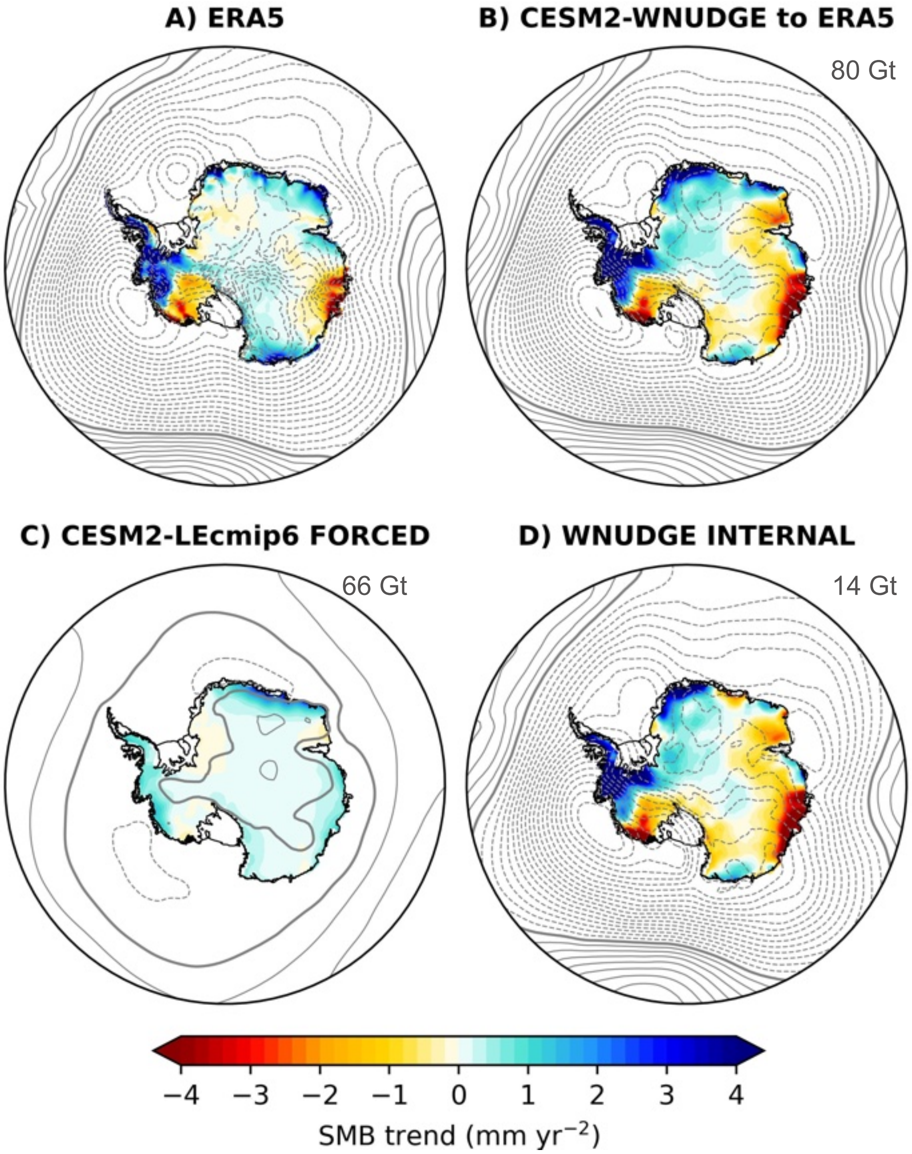

Fig. S9. Extension of Fig. 2 from the main text. ***(A)*** Precipitation minus evaporation and SLP trend in ERA5; ***(B)*** Result of nudging CESM2 to ERA5 winds; ***(C)*** The forced response in CESM2-LEcmip6 is removed from (B) to get the ***(D***) pattern that is due to wind nudging. All panels show trends for 2001-2022.

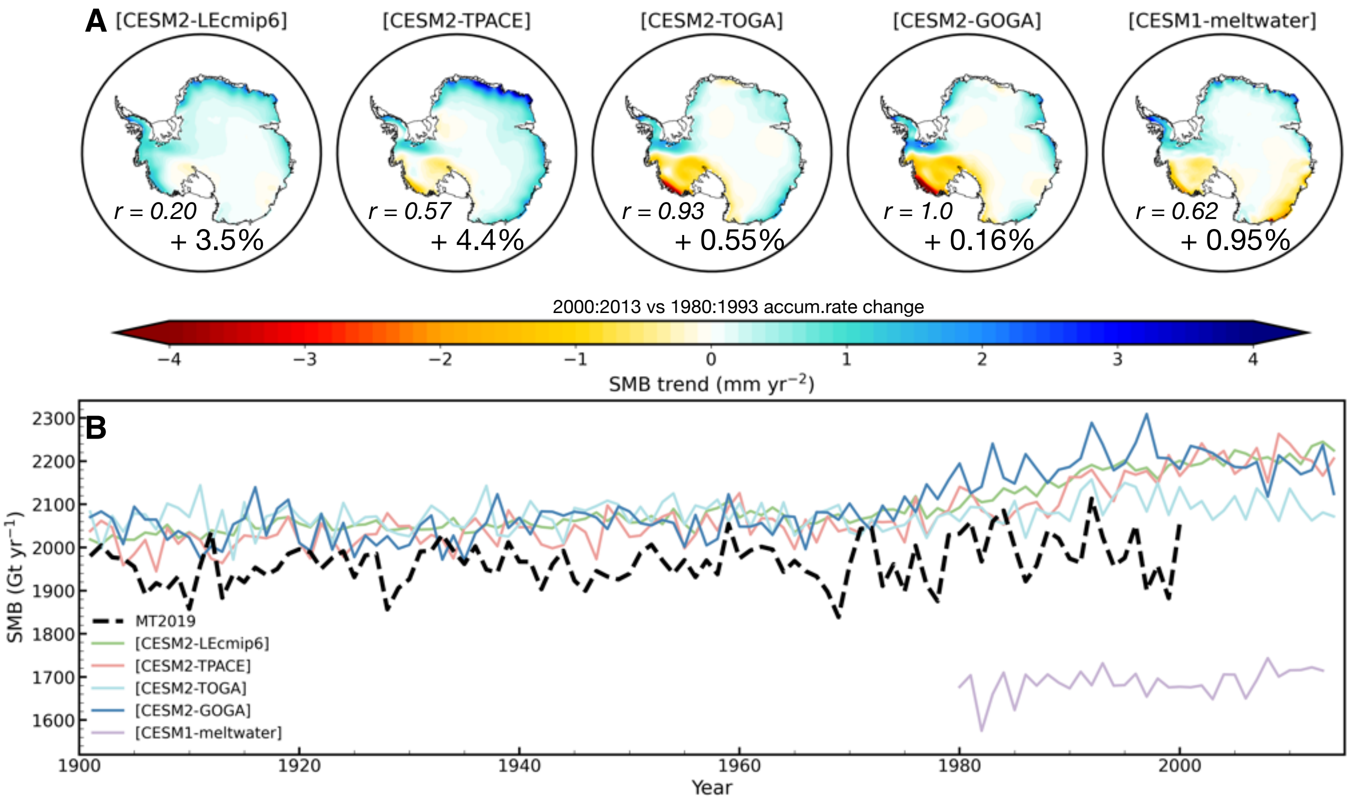

Fig. S10. ***(A)*** 1980-2013 trends in annual snow accumulation, according the ensemble means of the expirements indicated in the lables. Also shown is the percentage change in the Antarctic-wide accumation rate between the averages of (2000:2013) and (1980:1993), as well as the pattern correlation between the trend pattern given by [CESM2-GOGA] and the patterns in the respective maps. ***(B)*** Timeseries of Antarctic annual snow accumulation from the experiments indicated in the legend. The MT19 reconstruction is also shown.

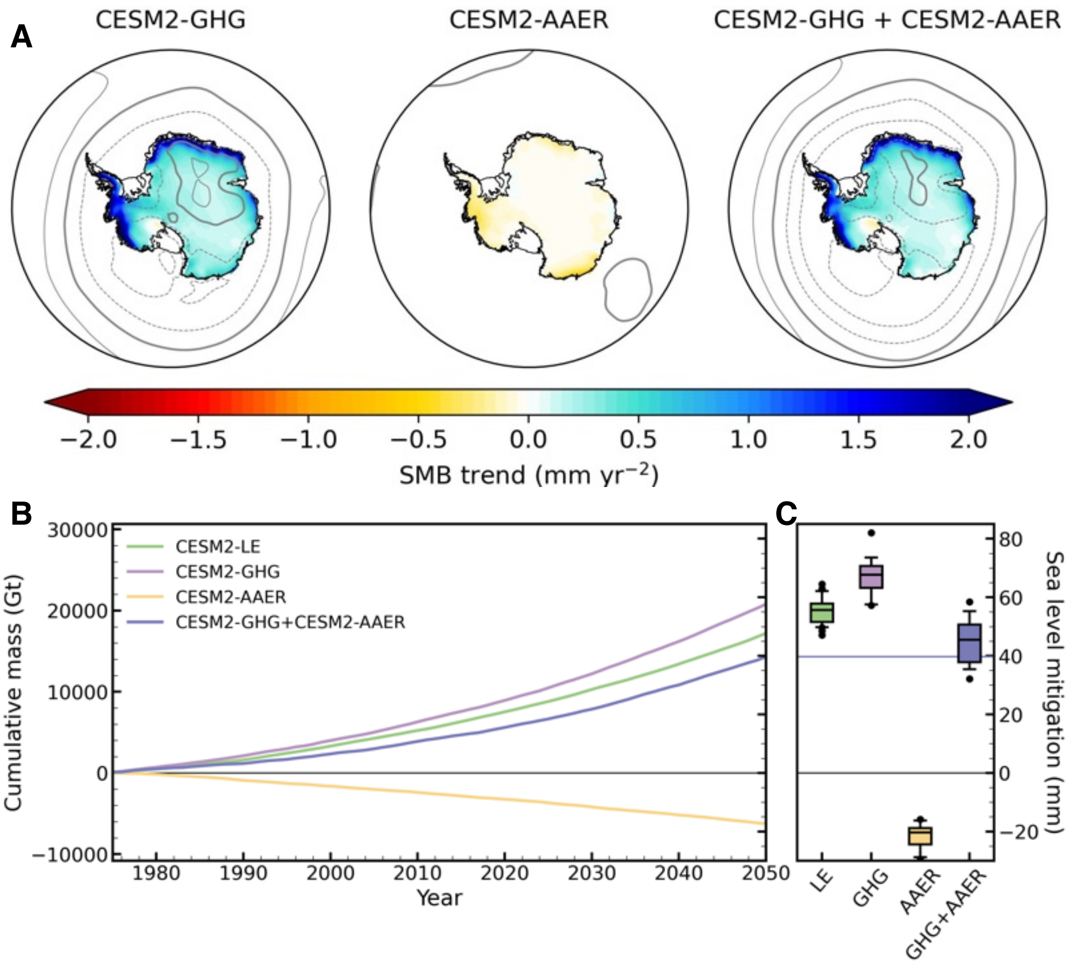

Fig. S11. ***(A)*** Projected snow accumulation (colorbar) and SLP (contours) trends 2001-2050; ***(B)*** Cumulative mass timeseries like in Fig. 1, but mass is accumulated since 1975 and extended to 2050; (***C)*** Box-whisker plot like in Fig 1, but for mass accumulated over 1901-2050, relative to the piControl. By comparison with Fig. 1*B*, this indicates that [GHG] + [AAER] projects ~30 mm of sea level mitigation over 2001-2050.

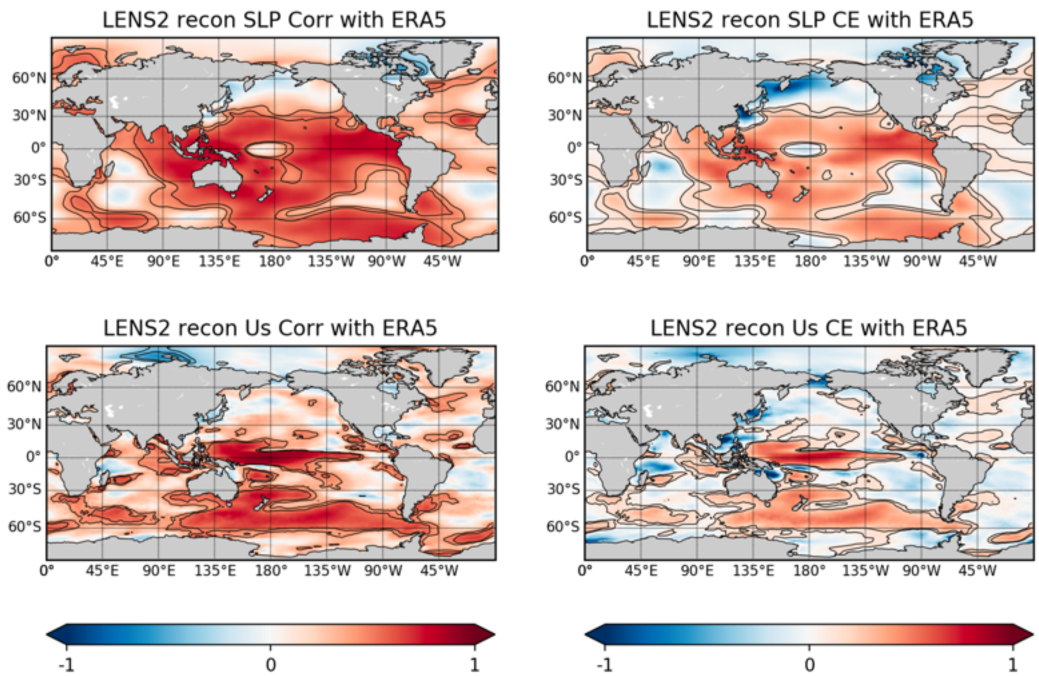

Fig. S12. Verification statistics for the CESM2-LE PDA reconstruction SLP (top row) and U10 (bottom row), compared to ERA5 reanalysis for the period of overlap, 1979 to 2005 (anomaly reference period used in this analysis is 1979 to 2005). Correlations are shown on the left, with contours highlighting p-values of 0.01 and 0.05. Coefficient of efficiency (CE) is shown on the right (>0 demonstrates skill).